

12 Strong Gravitational Lenses

Phil Marshall, Maruša Bradač, George Chartas, Gregory Dobler, Árdís Elíasdóttir, Emilio Falco, Chris Fassnacht, James Jee, Charles Keeton, Masamune Oguri, Anthony Tyson

LSST will contain more strong gravitational lensing events than any other survey preceding it, and will monitor them all at a cadence of a few days to a few weeks. Concurrent space-based optical or perhaps ground-based surveys may provide higher resolution imaging: the biggest advances in strong lensing science made with LSST will be in those areas that benefit most from the large volume and the high accuracy, multi-filter time series. In this chapter we propose an array of science projects that fit this bill.

We first provide a brief introduction to the basic physics of gravitational lensing, focusing on the formation of multiple images: the strong lensing regime. Further description of lensing phenomena will be provided as they arise throughout the chapter. We then make some predictions for the properties of samples of lenses of various kinds we can expect to discover with LSST: their numbers and distributions in redshift, image separation, and so on. This is important, since the principal step forward provided by LSST will be one of lens sample size, and the extent to which new lensing science projects will be enabled depends very much on the samples generated. From § 12.3 onwards we introduce the proposed LSST science projects. This is by no means an exhaustive list, but should serve as a good starting point for investigators looking to exploit the strong lensing phenomenon with LSST.

12.1 Basic Formalism

Árdís Elíasdóttir, Christopher D. Fassnacht

The phenomenon of strong gravitational lensing, whereby multiple images of a distant object are produced by a massive foreground object (hereafter the “lens”), provides a powerful tool for investigations of cosmology and galaxy structure. The 2006 Saas Fee lectures provide an excellent introduction to the physics of gravitational lenses (Schneider 2006; Kochanek 2006); we provide here a short summary of the basics. An extension of the discussion here with details more relevant to weak lensing can be found in Chapter 14.

12.1.1 The Lens Equation

The geometrical configuration of the lensing setup is most simply expressed in terms of angular diametric distances, which are defined so that “normal” Euclidean distance-angle relationships

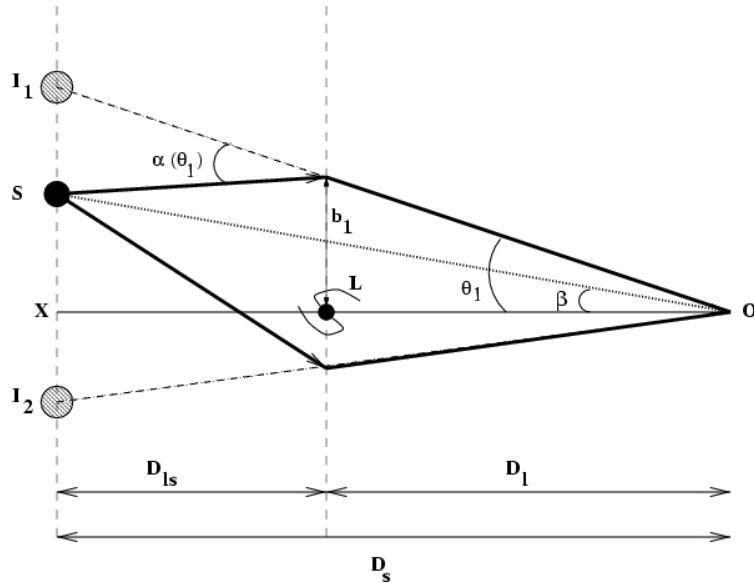


Figure 12.1: Cartoon showing lens configuration. The light coming from the source, S, is deflected due to the potential of the lensing object, L. D_l is the angular diameter distance from the observer to the lens, D_s is the angular diameter distance from the observer to the source and D_{ls} is the angular diameter distance from the lens to the source (note that $D_{ls} \neq D_s - D_l$). Due to the lensing effect, an observer O sees two images I_1 and I_2 of the original background source. The images are viewed at an angle θ which differs from the original angle β by the reduced deflection angle $\hat{\alpha}(\theta) = (D_{ls}/D_s)\alpha(\theta)$. The magnitude of the deflection angle α is determined by its impact parameter (b) and the distribution of mass in the lensing object. Figure from Fassnacht (1999).

hold. From Figure 12.1 one sees that for small angles

$$\alpha(\theta) D_{ls} + \beta D_s = \theta D_s \tag{12.1}$$

i.e.,

$$\beta = \theta - \hat{\alpha}(\theta) \tag{12.2}$$

where $\hat{\alpha}(\theta) \equiv \frac{D_{ls}}{D_s}\alpha(\theta)$ is the reduced deflection angle. Equation 12.2 is referred to as the lens equation, and its solutions θ give the angular position of the source as seen by the observer. It is in general a non-linear equation and can have multiple possible solutions of θ for a given source position β .

For a point mass M and perfect alignment between the observer, lens and source (i.e. $\beta = 0$), the solution to the lens equation is given by

$$\theta_E = \sqrt{\frac{D_{ls}}{D_l D_s} \frac{4GM}{c^2}}, \tag{12.3}$$

which defines a ring centered on the lens with angular radius, θ_E , called the Einstein radius. The Einstein radius defines the angular scale for a lensing setup, i.e., the typical separation of multiple images for a multiply imaged background source. For an extended mass distribution that has circular symmetry in its projected surface mass density, the Einstein ring radius is given by

$$\theta_E = \sqrt{\frac{D_{ls}}{D_l D_s} \frac{4GM(\theta_E)}{c^2}}, \tag{12.4}$$

where $M(\theta_E)$ is the projected mass contained within a cylinder of radius $R = D_1\theta_E$. For a galaxy, the typical Einstein radius is of the order of $1''$, while for galaxy clusters the Einstein radii are of the order of $10''$. This direct relationship between the Einstein ring radius and the mass of the lensing object provides a powerful method for making precise measurements of the masses of distant objects.

Various relations and quantities in lensing can be simplified by expressing them in terms of the projected gravitational potential. This potential, $\psi(\theta)$, is just the three-dimensional Newtonian gravitational potential of the lensing object, $\Phi(r)$, projected onto the plane of the sky and scaled:

$$\psi(\vec{\theta}) = \frac{D_{\text{ls}}}{D_1 D_s} \frac{2}{c^2} \int \Phi(D_1 \vec{\theta}, z) dz, \quad (12.5)$$

where z represents the coordinate along the line of sight. The scaled potential can also be written in terms of the mass surface density of the lensing object:

$$\psi(\theta) = \frac{1}{\pi} \int \kappa(\theta') \ln |\theta - \theta'| d^2\theta', \quad (12.6)$$

where κ is the dimensionless surface mass density (or convergence)

$$\kappa \equiv \Sigma / \Sigma_{\text{crit}}, \quad (12.7)$$

and Σ_{crit} is the ‘‘critical surface mass density’’ defined as

$$\Sigma_{\text{crit}} = \frac{c^2}{4\pi G} \frac{D_s}{D_1 D_{\text{ls}}}. \quad (12.8)$$

The distortion and magnification of the lensed images is given by the magnification tensor

$$M(\vec{\theta}) = A^{-1}(\vec{\theta}), \quad (12.9)$$

where

$$A(\vec{\theta}) = \frac{\partial \beta}{\partial \vec{\theta}} = \left(\delta_{ij} - \frac{\partial^2 \psi(\vec{\theta})}{\partial \theta_i \partial \theta_j} \right) = \begin{pmatrix} 1 - \kappa - \gamma_1 & -\gamma_2 \\ -\gamma_2 & 1 - \kappa + \gamma_1 \end{pmatrix} \quad (12.10)$$

is the Jacobian matrix and $\gamma \equiv \gamma_1 + \mathbf{i}\gamma_2$ is the shear (see also [Chapter 14](#)). The shape distortion of the lensed images is described by the shear while the magnification depends on both κ and γ .

12.1.2 The Fermat Potential and Time Delays

Another useful quantity is the Fermat potential, $\tau(\theta; \beta)$, defined as

$$\tau(\theta; \beta) = \frac{1}{2} (\theta - \beta)^2 - \psi(\theta), \quad (12.11)$$

which is a function of θ with β acting as a parameter. The lensed images form at the extrema of $\tau(\theta)$, namely at values of θ that satisfy the lens equation, [Equation 12.2](#), with the deflection angle $\alpha = \nabla_{\theta} \psi(\theta)$.

The travel time of the light ray is also affected by gravitational lensing. The delay compared to a light ray traveling on a direct path in empty space is given in terms of the Fermat potential (Equation 12.11) and equals

$$\Delta t = \frac{D_1 D_s}{c D_{ls}} (1 + z_l) \tau(\theta; \beta) + \text{constant}, \quad (12.12)$$

where z_l is the redshift of the lens plane and the constant arises from the integration of the potential along the travel path. The indeterminate constant term means that the time delay for a particular single image cannot be calculated. However, the *difference* in the travel time between two images, A and B , for a multiple imaged source can be measured, and is given by

$$\Delta t_{A,B} = \frac{D_1 D_s}{c D_{ls}} (1 + z_l) (\tau(\theta_A; \beta) - \tau(\theta_B; \beta)). \quad (12.13)$$

The time delay equation provides a direct link between the distribution of mass in the lens, which determines ψ , and the time delay, scaled by the factor outside the brackets on the right hand side of the equation, which is inversely proportional to H_0 through the ratio of angular diameter distances:

$$\frac{D_1 D_s}{D_{ls}} = \frac{1}{H_0} f(z_l, z_s, \Omega_m, \Omega_\Lambda). \quad (12.14)$$

The dependence of this ratio on the cosmological world model (Ω_m, Ω_Λ) is rather weak, changing by $\sim 10\%$ over a wide range of parameter choices. Thus, if $\Delta t_{A,B}$ can be measured and observations can constrain ψ for a given lens, the result is a determination of H_0 modulo the choice of (Ω_m, Ω_Λ). Conversely, if H_0 is known independently and $\Delta t_{A,B}$ is measured, the lens data provide clear information on the mass distribution of the lensing galaxy. This simple and elegant approach, developed by Refsdal (1964) long before the discovery of the first strong lens system, relies on a time variable background object such as an active galactic nucleus. LSST opens up the time domain in a way no previous optical telescope has: many of the most exciting LSST strong lenses will have variable sources.

12.1.3 Effects of the Environment

Frequently galaxy-scale lenses reside in dense environments and, therefore, it is necessary to consider not only the lensing effects of the main lensing object but also that of the environment. In modeling, these are referred to as “external convergence” and “external shear.”

To first order the external convergence can often be taken to be a constant over the relevant area (approximately $1''$ radius around the main lensing object for a galaxy-scale lens) and, therefore, cannot be separated from the convergence of the main lensing object. This is due to an effect called the “mass-sheet degeneracy,” which simply states that if $\kappa(\vec{\theta})$ is a solution to the lensing constraints (image positions) then $\kappa'(\vec{\theta}) = \lambda + (1 - \lambda)\kappa(\vec{\theta})$ is also a solution (where λ is a real number). The first term is equivalent to adding a constant convergence, hence the name “mass-sheet.” Additional information about the projected mass associated with the lens environment or density profile must be supplied in order to break this degeneracy: in practice, this can come from stellar dynamics, the image time delays plus an assumed Hubble constant, weak lensing measurements of the surrounding field, and so on. The external shear does have a non-degenerate effect on the image configuration, and is frequently needed in lens models to achieve satisfactory fits to the observational constraints.

12.2 Strong Gravitational Lenses in the LSST Survey

Masamune Oguri, Phil Marshall

LSST will discover an enormous number of strong gravitational lenses, allowing statistical studies and exploration of rare classes of lenses not at present possible with the small samples currently known. In 2009, when the first version of this book was published, strong lenses were still considered to be rather rare objects – in the LSST era this will no longer be the case. The large number of strong lenses expected to be found with LSST suggests that it will also be effective in locating rare, exotic strong lensing events (Figure 12.2). A big advantage of LSST will be its excellent image quality. The high spatial resolution is crucial for strong lens searches, as the typical angular scales of strong lensing are quite comparable to the seeing sizes of ground-based observations (see Figure 12.3).

In this section we give a brief overview of the samples of strong lenses we expect to find in the LSST database; these calculations are used in the individual project sections. We organize our projected inventory in order of increasing lens mass, dividing the galaxy-scale lenses by source type before moving on to groups and clusters of galaxies.

12.2.1 Galaxy-scale Strong Lenses

Most of the cross-section for strong gravitational lensing in the Universe is provided by massive elliptical galaxies (Turner et al. 1984). A typical object’s lensing cross-section is a strong function of its mass; the cross-section of an object is (roughly) proportional to its central velocity dispersion to the fourth power. However, the mass function is steep, and galaxies are far more numerous than the more massive groups and clusters – the total lensing optical depth peaks at around 220 km s^{-1} . The larger the cross-section of an object, the larger its Einstein radius; the predicted distribution of strong lens Einstein radii is shown in Figure 12.4.

A good approximation for computing the lensing rate at galaxy scales is then to focus on the massive galaxies. The observed SDSS velocity dispersion function (e.g., Choi et al. 2007) gives a measure of the number density of these objects at low redshift ($z \sim 0.1$ or so). We must expect this mass function to have evolved since redshift 1, but perhaps not by much – attempts to use the observed numbers of lenses as a way of measuring cosmic volume (and hence, primarily, Ω_Λ), get answers for the cosmological parameters in agreement with other cosmographic probes without having to make any such evolution corrections (e.g., see Mitchell et al. 2005; Oguri et al. 2008).

The simplest realistic model for a galaxy mass distribution is the elliptical extension of the singular isothermal sphere $\rho(r) \propto r^{-2}$, namely the singular isothermal ellipsoid (e.g. Kormann et al. 1994):

$$\kappa(\theta) = \frac{\theta_E}{2} \frac{1}{\sqrt{(1-e)x^2 + (1-e)^{-1}y^2}}, \quad (12.15)$$

$$\theta_E = 4\pi \left(\frac{\sigma}{c}\right)^2 \frac{D_{ls}}{D_s}. \quad (12.16)$$

This turns out to be remarkably accurate for massive galaxies that *are* acting as strong lenses (see e.g., Rusin & Kochanek 2005; Koopmans et al. 2006). For our model lenses, the ellipticity of the



Figure 12.2: Lensed quasar SDSS J1004+4112 (Inada et al. 2003). Shown is a color-composite HST image from <http://hubblesite.org/newscenter/archive/releases/2006/23/>. The lens is a cluster of galaxies, giving rise to five images with a maximum separation of $15''$. LSST will act as a *finder* for exotic objects such as this.

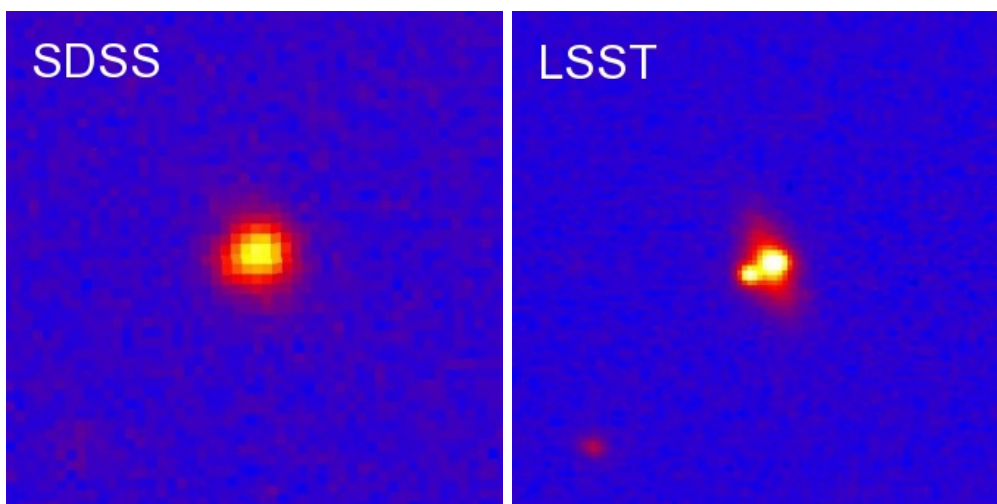


Figure 12.3: A comparison of the images of gravitationally lensed quasars. The left panel shows the image of SDSS J1332+0347 (Morokuma et al. 2007) (a double lens with a separation of $1.14''$) obtained by the SDSS (median seeing of $1.4''$), while the right panel shows an image of the same object taken with Suprime-Cam on Subaru, with seeing of $0.7''$, comparable to that of LSST. The drastic difference of appearance between these two images demonstrates the importance of high spatial resolution for strong lens searches.

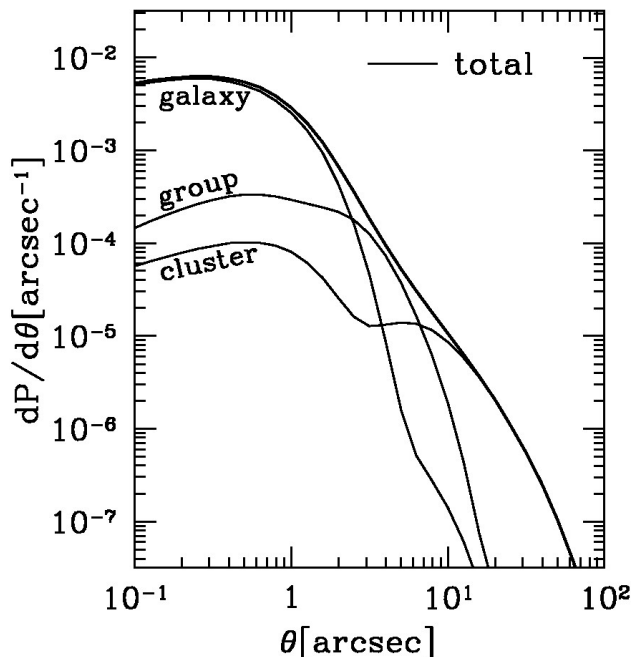


Figure 12.4: The distribution of lens image separations (approximately twice the Einstein radius) for three different scales: galaxy, group, and cluster-scales, predicted by a halo model (figure from [Oguri 2006](#)). The total distribution is shown by the thick line.

lenses is assumed to be distributed as a Gaussian with mean of 0.3 and scatter of 0.16. We also include external shear, with median of 0.05 and scatter of 0.2 dex, which is the level expected in ray-tracing simulations (e.g., [Dalal 2005](#)). The orientation of the external shear is taken to be random.

Given the lens ellipticity and external shear distribution, together with a suitable distribution of background sources, we can now calculate the expected galaxy-scale lens abundance. We consider three types of sources: faint blue galaxies, quasars and AGN, and supernovae. Of course the latter two also have host galaxies – but these may be difficult to detect in the presence of a bright point source. As we will see, in a ground-based imaging survey, time-variable point-like sources are the easiest to detect.

Galaxy-Galaxy Strong Lenses

We expect the galaxy-scale lens population to be dominated by massive elliptical galaxies at redshift 0.5–1.0, whose background light sources are the ubiquitous faint blue galaxies. The typical gravitational lens, therefore, looks like a bright red galaxy, with some residual blue flux around it. The detection of such systems depends on our ability to distinguish lens light from source light – this inevitably means selecting against late-type lens galaxies, whose blue disks provide considerable confusion. An exception might be edge-on spirals: the high projected masses make for efficient lenses and the resulting cusp-configuration arcs are easily recognizable.

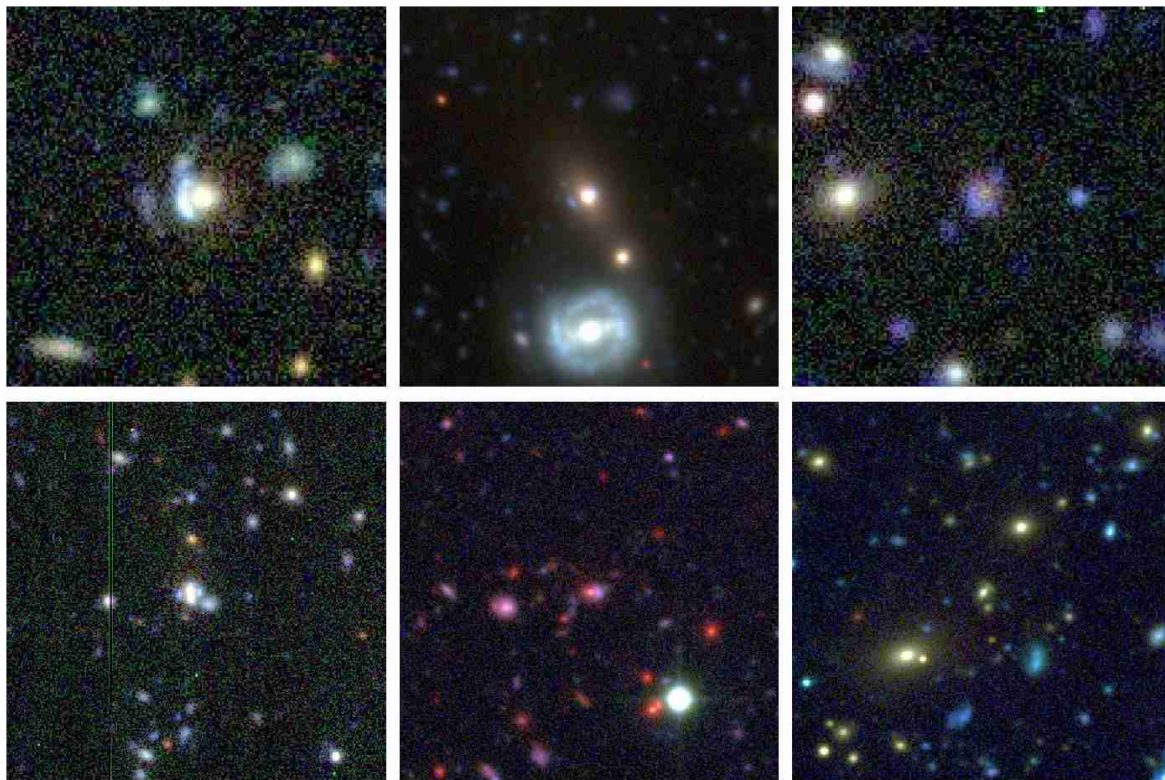


Figure 12.5: Galaxy-scale strong lenses detected in the CFHTLS images, from the sample compiled by Gavazzi et al. (in prep.). All were confirmed by high resolution imaging with HST. Color images kindly provided by R. Cabanac and the SL2S collaboration.

The SLACS survey has provided the largest sample of galaxy-scale lenses to date, with almost 100 lenses detected and measured (Bolton et al. 2008): the sources are indeed faint blue galaxies, selected by their emission lines appearing in the (lower redshift) SDSS luminous red galaxy spectra. Due to their selection for spectroscopic observation, the lens galaxies tend to be luminous elliptical galaxies at around redshift 0.2. Extending this spectroscopic search to the SDSS-III “BOSS” survey should increase this sample by a factor of two or more (A. Bolton, private communication), to cover lens galaxies at somewhat higher redshift. Optical imaging surveys are beginning to catch up, with various HST surveys beginning to provide samples of several tens of lenses (e.g., Moustakas et al. 2007; Faure et al. 2008, Marshall et al. in preparation). From the ground, the SL2S survey is finding similar numbers of galaxy-scale lenses in the CFHTLS survey area (Cabanac et al. 2007).

Figure 12.5 shows a gallery of galaxy-galaxy lenses detected in the CFHT legacy survey images by the SL2S project team (Cabanac et al. 2007, Gavazzi et al. in preparation). This survey is very well matched to what LSST will provide: the 4 deg^2 field is comparable in depth to the LSST 10-year stack, while the 170 deg^2 wide survey is not much deeper than a single LSST visit.¹

The SL2S galaxy-scale lens sample contains about 15 confirmed gravitational lenses or about 0.1

¹The service-mode CFHTLS is quite uniform, having image quality around $0.9''$ with little scatter. The “best-seeing” stack has image quality closer to $0.65''$. With LSST we expect median seeing of better than $0.7''$ (Figure 2.3), but a broader distribution of PSF widths.

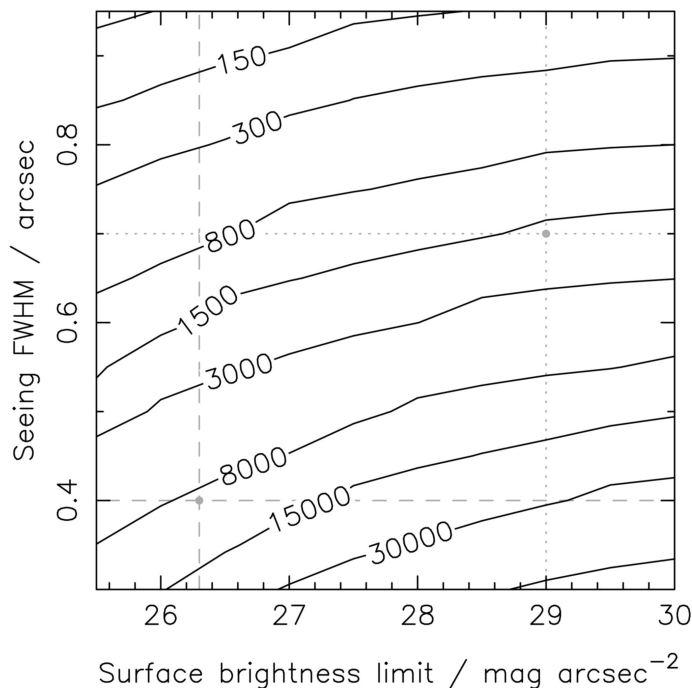


Figure 12.6: Number of galaxy-galaxy strong lenses expected in the 20,000 deg² LSST survey, as a function of seeing FWHM and surface brightness limit. The dashed lines show the approximate expected surface brightness limit for one visit and the approximate seeing FWHM in the best visit's image. The dotted lines mark the median seeing for the survey and the approximate surface brightness limit of the 10-year stacked image.

deg⁻². Higher resolution imaging (from HST) was used to confirm the lensing nature of these objects, at a success rate of about 50%. The number of cleanly detected CFHT-only lenses is rather lower, perhaps just a handful of cases in the whole 170 deg² survey. This is in broad agreement with a calculation like that described above, once we factor in the need to detect the lens features above the sky background. The results of this calculation are shown in Figure 12.6, which shows clearly how the detection rate of galaxy-scale strong lenses is a strong function of image quality. The right-hand dotted cross-hair shows the expected approximate image quality and surface brightness limit of the 10-year stack, or equivalently, the Deep CFHTLS fields, and suggests a lens detection rate of 0.075 per square degree. The left-hand cross-hair shows the surface brightness limit of a single LSST visit, and the best expected seeing. By optimizing the image analysis (to capitalize on both the resolution and the depth) we can expect to discover $\sim 10^4$ galaxy-galaxy strong lenses in the 10-year 20,000 deg² LSST survey. The challenge is to make the first cut efficient: fitting simple models to galaxy images for photometric and morphological studies will leave residuals that contain information allowing lensing to be detected, but these residuals will need to be both available and well-characterized. This information is also required by, for example, those searching for galaxy mergers (§ 9.9). Given its survey depth, the Dark Energy Survey (DES) should yield a number density of lenses somewhere in between that of the CFHTLS Wide and Deep fields, and so in its 4000 deg² survey area DES will discover at least a few hundred strong galaxy-galaxy lenses. Again, this number would increase with improved image quality and analysis.

In § 12.3 below we describe the properties of these lenses, and their application in galaxy evolution

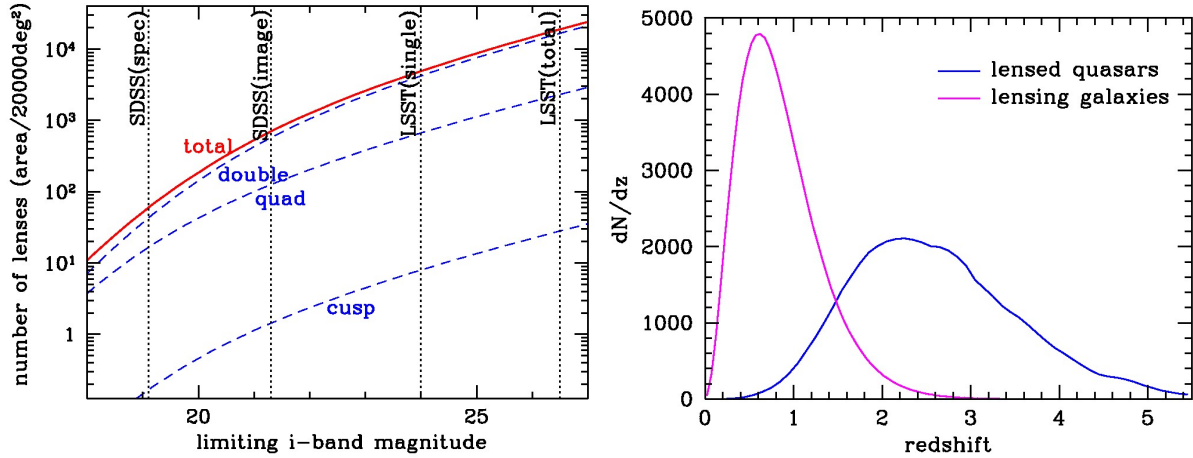


Figure 12.7: The number of lensed quasars expected in LSST. *Left:* The number of lenses in 20,000 deg² region as a function of i -band limiting magnitude. Dashed lines are numbers of lenses for each image multiplicity (double, quadruple, and three-image naked cusp lenses). The total number is indicated by the red solid line. Limiting magnitudes in SDSS and LSST are shown by vertical dotted lines. *Right:* The redshift distributions of lensed quasars (*blue*) and lensing galaxies (*magenta*) adopting $i_{\text{lim}} = 24$.

science.

Galaxy-scale Lensed Quasars

Galaxy-scale lensed quasars were the first type of strong lensing to be discovered (Walsh et al. 1979); the state of the art in lensed quasar searching is the SDSS quasar lens survey (Oguri et al. 2006), which has (so far) found 32 new lensed quasars and rediscovered 13 more. The bright and compact nature of quasars makes it relatively easy to locate and characterize such strong lens systems (see Figure 12.3 for an example). An advantage of lensed quasars is that the sources are very often variable: measurable time delays between images provide unique information on both the lens potential and cosmology (see § 12.4 and § 12.5). We expect that lensed quasars in LSST will be most readily detected using their time variability (Kochanek et al. 2006a). In § 12.8 we also discuss using strong lenses to provide a magnified view of AGN and their host galaxies.

We compute the expected number of lensed quasars in LSST as follows. We first construct a model quasar luminosity function of double-power-law form, fit to the SDSS results of Richards et al. (2006), assuming the form of the luminosity evolution proposed by Madau et al. (1999). To take LSST observable limits into account, we reject lenses with image separation $\theta < 0.5''$, and only include those lenses whose fainter images (the third brightest images for quads) have $i < 24.0$. Thus these objects will be detectable in each visit, and thus recognizable by their variability. This will also allow us to measure time delays in these objects.

Figure 12.7 shows the number of lensed quasars expected in LSST as a function of limiting magnitude. We expect to find ~ 2600 well-measured lensed quasars. Thus the LSST lensed quasar sample will be nearly two orders of magnitude larger than the current largest survey of lensed quasars. There are expected to be as many as $\sim 10^3$ lensed quasars detectable in the PS1 3π survey, but these will have only sparsely-sampled light curves (six epochs per filter in three years). The 4000

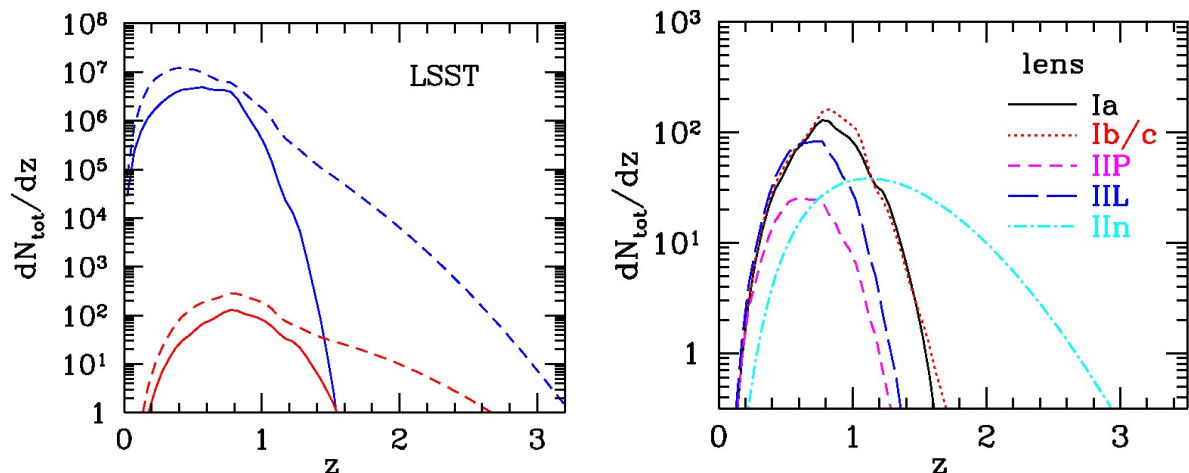


Figure 12.8: The abundance of expected lensed SNe observed with the 10-year LSST survey as a function of the redshift. The left panel shows the unlensed population in blue, for comparison. Dashed curves show core-collapse SNe, solid curves type Ia SNe. In the right panel, the contribution of each SN type to the number of lensed SNe is shown.

deg² DES should also contain ~ 500 lensed quasars, but with no time variability information to aid detection or to provide image time delay information.

The calculation above also predicts the distribution of image multiplicity. In general, the number of quadruple lenses decreases with increasing limiting magnitude, because the magnification bias becomes smaller for fainter quasars. For the LSST quasar lens sample, the fraction of quadruple lenses is predicted to be $\sim 14\%$. The lensed quasars are typically located at $z \sim 2 - 3$, where the space density of luminous quasars also peaks (e.g., [Richards et al. 2006](#)). The lensing galaxies are typically at $z \sim 0.6$, but a significant fraction of lensing is produced by galaxies at $z > 1$. We discuss this in the context of galaxy evolution studies in [§ 12.3](#).

Galaxy-scale Lensed Supernovae

Strongly lensed supernovae (SNe) will provide accurate estimates of time delays between images, because we have an a priori understanding of their light curves. Furthermore, the SNe fade, allowing us to study the structure of the lensing galaxies in great detail.

We calculate the number of lensed SNe as follows. First we adopt the star formation rate from [Hopkins & Beacom \(2006\)](#), assuming the initial mass function of [Baldry & Glazebrook 2003](#)). The Ia rate is then computed from the sum of “prompt” and “delay” components, following [Sullivan et al. \(2006\)](#), see the discussion in [§ 11.8](#)). The core-collapse supernova (SN) rate is assumed to be simply proportional to the star-formation rate ([Hopkins & Beacom 2006](#)). For the relative rate of the different types of core-collapse supernovae (Ib/c, IIP, IIL, IIn), we use the compilation in [Oda & Totani \(2005\)](#). The luminosity functions of these SNe are assumed to be Gaussians (in magnitude) with different means and scatters, which we take from [Oda & Totani \(2005\)](#). For lensed SNe to be detected by LSST, we assume that the i -band peak magnitude of the fainter image must be brighter than $i = 23.3$, which is a conservative approximation of the 10σ point

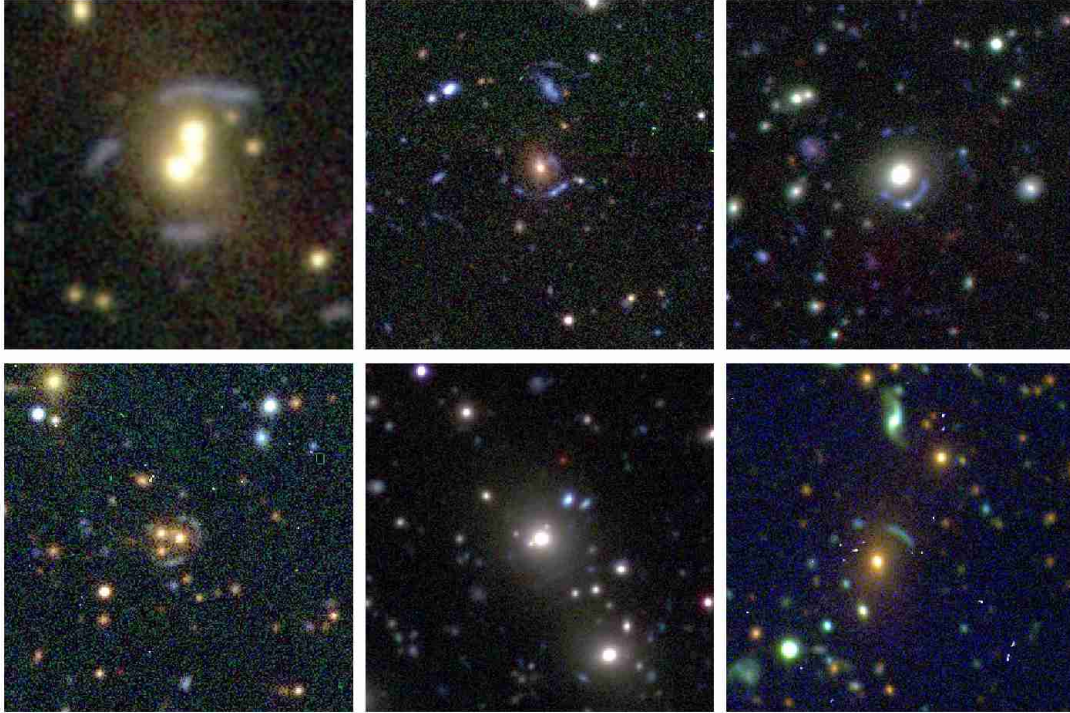


Figure 12.9: Group-scale strong lenses detected in the CFHTLS images, from the sample compiled by [Limousin et al. \(2008\)](#). Color images kindly provided by R. Cabanac and the SL2S collaboration.

source detection limit for a single visit. We insist the image separation has to be larger than $0.5''$ for a clean identification, arguing that the centroiding of the lens galaxy, and first image, will be good enough that the appearance of the second image will be a significantly strong trigger to justify confirmation follow-up of some sort. We return to the issues of detecting and following-up lensed SNe in § 12.5. We assume that each patch of the sky is well sampled for three months during each year; thus for a 10-year LSST survey the effective total monitoring duration of the SN search is 2.5 years. The right-hand panel of [Figure 12.8](#) shows the expected total number of strongly lensed SNe in the 10-year LSST survey, as a function of redshift, compared to their parent SN distribution. It is predicted that 330 lensed SNe will be discovered in total, 90 of which are type Ia and 240 are core-collapse SNe. Redshifts of lensed SNe are typically ~ 0.8 , while the lenses will primarily be massive elliptical galaxies at $z \sim 0.2$. Similar distributions may be expected for DES and PS1 prior to LSST – but the numbers will be far smaller due to the lower resolution and depth (PS1) or lack of cadence (DES). While we may expect the first discovery of a strongly lensed supernova to occur prior to LSST, they will be studied on an industrial scale with LSST.

12.2.2 Strong Lensing by Groups

Strong lensing by galaxy groups has not been studied very much to date, because finding group-scale lensing requires a very wide field survey. Galaxy groups represent the transition in mass between galaxies and clusters, and are crucial to understand the formation and evolution of massive

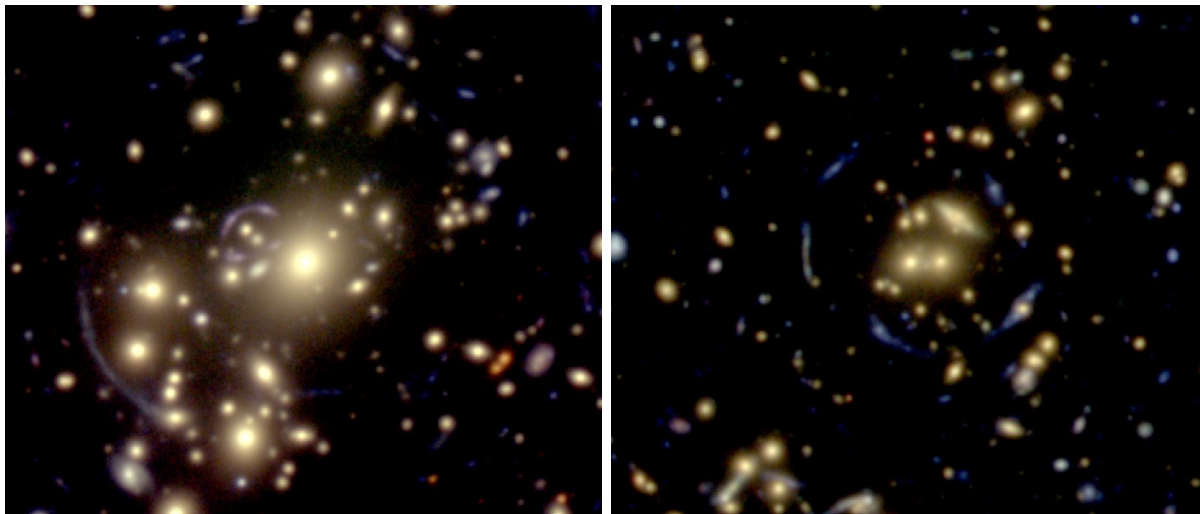


Figure 12.10: Example of giant arcs in massive clusters. Color composite Subaru Suprime-cam images of clusters Abell 1703 and SDSS J1446+3032 are shown (Oguri et al. 2009).

galaxies. Limousin et al. (2008) presented a sample of 13 group-scale strong lensing from the SL2S (see Figure 12.9), and used it to explore the distribution of mass and light in galaxy groups. By extrapolating the SL2S result (see also Figure 12.4), we can expect to discover $\sim 10^3$ group-scale strong lenses in the 10-year LSST survey. Strong lensing by groups is often quite complicated, and thus is a promising site to look for exotic lensing events such as higher-order catastrophes (Orban de Xivry & Marshall 2009). This is an area where DES and PS1 are more competitive, at least for the bright, easily followed-up arcs. LSST, like CFHTLS, will probe to fainter and more numerous arcs.

12.2.3 Cluster Strong Lenses

Since the first discovery of a giant arc in cluster Abell 370 (Lynds & Petrosian 1986; Soucail et al. 1987), many lensed arcs have been discovered in clusters (Figure 12.10). The number of lensed arcs in a cluster is a strong function of the cluster mass, such that the majority of the massive clusters ($> 10^{15} M_{\odot}$) exhibit strongly lensed background galaxies when observed to the depth achievable in the LSST survey (e.g., Broadhurst et al. 2005). Being able to identify systems of multiple images via their colors and morphologies, requires high resolution imaging. It is here that LSST will again have an advantage over precursor surveys like DES and PS1.

In Figure 12.11 we plot estimates for the number of multiple-image systems produced by massive clusters. As can be seen in this plot, we can expect to detect several thousand massive clusters in the stacked image set whose Einstein radii are $10''$ or greater. Not all will show strong lensing: the number of multiple image systems detectable with LSST is likely to be ~ 1000 , but with the more massive clusters being more likely to host many multiple image systems. Very roughly, we expect that clusters with Einstein radius greater than $\sim 30''$ should host more than one strong lens system detectable by LSST: there will be ~ 50 such massive systems in the cluster sample. Given the relative scarcity of these most massive clusters, we consider the sample of LSST strong lensing

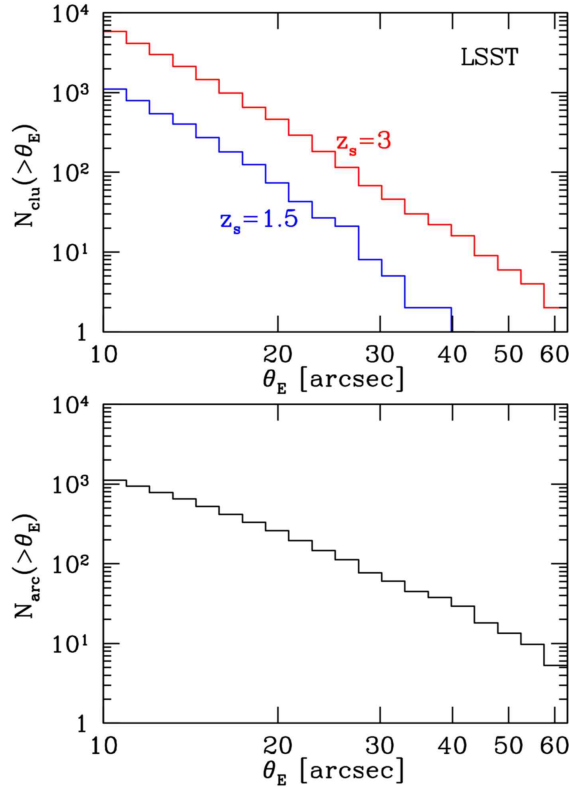


Figure 12.11: Estimated numbers of clusters with larger Einstein radii (top) and cluster multiple image systems (bottom) in the $i = 27$ LSST survey, based on the semi-analytic model of Oguri & Blandford (2009), which assumes smooth triaxial halos as lensing clusters. Here we consider only clusters with $M > 10^{14} M_{\odot}$. The background galaxy number density is adopted from Zhan et al. (2009). Although our model does not include central galaxies, the effect of the baryonic concentration is not very important for our sample of lensing clusters with relatively large Einstein radius, $> 10''$. The magnification bias is not included, which provides quite conservative estimates of multiple image systems. The number of multiple image systems available is of order 10^3 , with these systems roughly evenly divided over a similar number of clusters.

clusters to number 1000 or so, with the majority displaying a single multiple image system (arcs and counter arcs). This number is quite uncertain: the detectability and identifiability of strongly lensed features is a strong function of source size, image quality, and the detailed properties of cluster mass distributions: detailed simulations will be required to understand the properties of the expected sample in more detail, and indeed to reveal the information likely to be obtained on cluster physics and cosmology based on arc statistics.

Strong lensing by clusters is enormously useful in exploring the mass distribution in clusters. For instance, merging clusters of galaxies serve as one of the best astronomical sites to explore properties of dark matter (§ 12.10). Strong lensing provides robust measurements of cluster core masses and, therefore, by combining them with weak lensing measurements, one can study the density profile of clusters over a wide range in radii, which provides another test of structure formation models (§ 12.12). Once the mass distribution is understood, we can then use strong lensing clusters to find and measure distant faint sources by making use of these high magnification and low background “cosmic telescopes” (§ 12.11).

12.3 Massive Galaxy Structure and Evolution

Phil Marshall, Christopher D. Fassnacht, Charles R. Keeton

The largest samples of strong lenses discovered and measured with LSST will be galaxy-scale objects (§ 12.2), which (among other things) will allow us to measure lens galaxy mass. In this section we describe several approaches towards measuring the gross mass structure of massive galaxies, allowing us to trace their evolution since they were formed.

12.3.1 Science with the LSST Data Alone

Optimal combination of the survey images should permit:

- accurate measurements of the image positions ($\pm 0.05''$), fluxes, and time delays (\pm few days) for several thousand (§ 12.2) lensed quasars, AGN, and supernovae and
- detection and associated modeling, of $\simeq 10^4$ lensed galaxies.

The multi-band imaging will yield photometric redshift estimates for the lens and source. The most robust output from all these data will be the mass of the lens galaxy enclosed within the Einstein radius. When combined with the photometry, this provides an accurate aperture mass-to-light ratio for each strong lens galaxy regardless of its redshift. Rusin & Kochanek (2005, and references therein) illustrate a method to use strong lens ensembles to probe the mean density profile and luminosity evolution of early-type galaxies. The current standard is the SLACS survey (Bolton et al. 2006, 2008, and subsequent papers): with 70 spectroscopically-selected low redshift (median 0.2), luminous lenses observed with HST, the SLACS team was able to place robust constraints on the mean logarithmic slope of the density profiles (combining the lensing image separations with the SDSS stellar velocity dispersions). However, the first thing we can do with LSST lenses is increase the ensemble size from tens to thousands, pushing out to higher redshifts and lower lens masses.

Note the distinction between *ensemble* studies that do not require statistical completeness and *statistical* studies that do. LSST will vastly expand both types of samples. Statistical studies will be more easily carried out with the lensed quasar sample, where the selection function is more readily characterized. The larger lensed galaxy sample will require more work to render its selection function.

The first thing we can do with a large, statistically complete sample from LSST is measure the mass function of lens galaxies. Since we know the weighting from the lensing cross section, we will be able to probe early-type (and, with fewer numbers, other types!) galaxy mass evolution over a wide range of redshift, up to and including the era of elliptical galaxy formation ($z_1 \simeq 1 - 2$). From the mock catalogue of well-measured lensed quasars described in § 12.2.1, we expect about 25% ($\simeq 600$) of the lenses to lie at $z_d > 1$, and 5% ($\simeq 140$) to lie at $z_d > 1.5$, if the assumption of a non-evolving velocity function is valid to these redshifts. While it seems to be a reasonable model at lower redshifts (Oguri et al. 2008), it may not be at such high redshifts: the high- z lenses are sensitive probes of the evolving mass function.

The time delays contain information about the density profiles of the lensing galaxies although it is combined with the Hubble parameter (Kochanek 2002). Kochanek et al. (2006b) fixed H_0 and then used the time delays in the lens HE 0435–1223 to infer that the lens galaxy has a density profile that is shallower than the mean, quasi-isothermal profile of lens galaxies. With the LSST ensemble we can consider simultaneously fitting for H_0 and the mass density profile parameters of the galaxy population (see § 12.4 and § 12.5 for more discussion of strong lens cosmography).

The lensed quasar sample has a further appealing property: it will be selected by the properties of the sources, not the lenses. When searching for lensed *galaxies* in ground-based imaging data, the confusion between blue arcs and spiral arms is severe enough that one is often forced to focus on elliptical galaxy lens candidates. In a source-selected lensed *quasar*, however, the lens galaxies need not be elliptical, or indeed regular in any way. This means we can aspire to compile samples of massive lens galaxies at high redshift that are to first order selected by their mass.

Understanding the distribution of galaxy density profiles out to $z \sim 1$ will strongly constrain models of galaxy formation, including both the hierarchical formation picture (what range of density profiles are expected if ellipticals form from spiral mergers?) and environmental effects such as tidal stripping (how do galaxy density profiles vary with environment?). In this way, we anticipate LSST providing the best assessment of the distribution of galaxy mass density profiles out to $z \sim 1$.

12.3.2 Science Enabled by Follow-up Data

While the LSST data will provide a wealth of new lensing measurements, we summarize very briefly some of the additional opportunities provided by various follow-up campaigns:

- **Spectroscopic redshifts.** While the LSST photometric redshifts will be accurate to $0.04(1+z_l)$ for the lens galaxies (§ 3.8.4), the source redshifts will be somewhat more uncertain. High accuracy mass density profiles will require spectroscopic redshifts. Some prioritization of the sample may be required: we can imagine, for example, selecting the most informative image configuration lenses in redshift bins for spectroscopic follow-up.
- **Combining lensing and stellar dynamics.** Stellar velocity dispersions provide valuable additional information on galaxy mass profiles, to first order providing an additional aperture mass estimate at a different radius to the Einstein radius (see e.g., Treu & Koopmans 2004; Koopmans et al. 2006; Trott et al. 2008). More subtly the stellar dynamics probe the three-dimensional potential, while the lensing is sensitive to mass in projection, meaning that some degeneracies between bulge, disk, and halo can be broken. Again, since these measurements are expensive, we can imagine focusing on a particular well-selected subset of LSST lenses.
- **High resolution imaging.** The host galaxies of lensed quasars may appear too faint in the survey images – but distorted into Einstein rings, they provide valuable information on the lens mass distribution. They are also of interest to those interested in the physical properties of quasar host galaxies, since the lensing effect magnifies the galaxy, making it much more easily studied than it otherwise would be.
- **Infrared imaging.** There is an obvious synergy with concurrent near-infrared surveys such as VISTA and SASIR. Infrared photometry will enable the study of lens galaxy stellar populations; one more handle on the mass distributions of massive galaxies.

Note that the study of massive galaxies and their evolution with detailed strong lensing measurements can be done simultaneously with the cosmographic study discussed in § 12.4: there will be some considerable overlap between the cosmographic lens sample and that defined for galaxy evolution studies. The optimal redshift distribution for each ensemble is a topic for research in the coming years.

12.4 Cosmography from Modeling of Time Delay Lenses and Their Environments

Christopher D. Fassnacht, Phil Marshall, Charles R. Keeton, Gregory Dobler, Masamune Oguri

12.4.1 Introduction

Although gravitational lenses provide information on many cosmological parameters, historically the most common application has been the use of strong lens time delays to make measurements of the distance scale of the Universe, via the Hubble Constant, H_0 (Equation 12.13). The current sample of lenses with robust time delay measurements is small, ~ 20 systems or fewer, so that the full power of statistical analyses cannot be applied. In fact, the sample suffers from further problems in that many of the lens systems have special features (two lensing galaxies, the lens galaxy sitting in a cluster potential, and so on) that complicate the lens modeling and would conceivably lead to their being rejected from larger samples. The large sample of LSST time delay lenses will enable the selection of subsamples that avoid these problems. These subsamples may be those showing promising signs of an observable point source host galaxy distorted into an Einstein ring, those with a particularly well-understood lens environment, those with especially simple lens galaxy morphology. While all current time delay lenses have AGN sources, a significant fraction of the LSST sample will be lensed supernovae (§ 12.2.1). These will be especially useful if the lensed supernova is a Type Ia, where it may be possible to directly determine the magnification factors of the individual images.

In § 12.2 we showed that the expected sizes of the LSST samples of well-measured lensed quasars and lensed supernovae are some 2600 and 330 respectively; 90 of the lensed SNe are expected to be type Ia. Assuming the estimated quad fraction of 14%, we can expect to have some 400 quadruply-imaged variable sources to work with. Cuts in environment complexity and lens morphology will reduce this further – a reasonable goal would be to construct a sample of 100 or more high quality time delay lenses for cosmographic study. From simple counting statistics this represents an order of magnitude increase in *precision* over the current sample.

We can imagine studying this cosmographic sample in some detail: with additional information on the lens mass distribution coming from the extended images observed at higher resolution (with JWST or ground-based adaptive optics imaging) and from spectroscopic velocity dispersion measurements, and with spectroscopically-measured lens and source redshifts, we can break some of the modeling degeneracies and obtain quite tight constraints on H_0 given an assumed cosmology (e.g., Koopmans et al. 2003). With a larger sample, we can imagine relaxing this assumption and

providing an independent cosmological probe competitive with those from weak lensing (Chapter 14), supernovae (Chapter 11), and BAO (Chapter 13). Note that the approach described here is complementary to the statistical method of § 12.5, which aims to use much larger numbers of individually less-informative (often double-image) lenses.

12.4.2 H_0 and the Practicalities of Time Delay Measurements

As shown in Equation 12.13, the measurement of H_0 using a strong lens system requires that the time delay(s) in the system be measured. In the past, this has been a challenging exercise. The measurement of time delays relies on regular monitoring of the lens system in question. Depending on the image configuration and the mass of the lens, time delays can range from hours to over a year. The monitoring should return robust estimates of the image fluxes for each epoch. This can be easily achieved in the monitoring of radio-loud lenses (e.g., Fassnacht et al. 2002), where contamination from the lensing galaxy is typically not a concern. With optical monitoring, however, the fluxes of the lensed AGN images must be cleanly disentangled from the emission from the lensing galaxy itself. The standard difference imaging pipeline may not provide accurate enough light curves, and in most cases we anticipate needing to use the high resolution exposures to inform the photometry in the poorer image quality exposures: to achieve this, fitting techniques such as those developed by Courbin et al. (1998) or Burud et al. (2001) must be employed. These techniques are straightforwardly extended to incorporate even higher-resolution follow-up imaging (e.g., from HST or adaptive optics) of the system as a basis for the deconvolution of the imaging.

Once obtained, the light curves must be evaluated to determine the best-fit time delays between the lensed components. The statistics of time delays has a rich history (e.g., Press et al. 1992a,b; Pelt et al. 1994, 1996), driven in part by the difficulty in obtaining a clean delay from Q0957+561 (the first lensed quasar discovered) until a sharp feature was finally seen in the light curves (Kundić et al. 1995, 1997). Most lens monitoring campaigns do not obtain regular sampling; dealing properly with unevenly sampled data is a crucial part of a successful light curve analysis. Two successful approaches are the “dispersion” method of Pelt et al. (1994, 1996), which does not require any data interpolation, and fitting of smooth functions to the data (e.g., Legendre polynomials; Kochanek et al. 2006b). With these approaches and others, time delays have now been successfully measured in ~ 15 lens systems (e.g., Barkana 1997; Biggs et al. 1999; Lovell et al. 1998; Koopmans et al. 2000; Burud et al. 2000, 2002b,a; Fassnacht et al. 2002; Hjorth et al. 2002; Kochanek et al. 2006b; Vuissoz et al. 2007, 2008). Figure 12.12 shows an example of light curves from a monitoring program that led to time delay measurements in a four-image lens system.

It is yet to be seen what time delay precision the LSST cadence will allow: experiments with simulated image data need to be performed based on the operations simulator output. We note that the proposed main survey cadence (§ 2.1) leads to an exposure in some filter being taken every week (or less) for an observing season of three months or so. This cadence is not very different from the typical optical monitoring campaigns referred to above. However, the length of the monitoring season is significantly shorter, as lens monitoring campaigns are typically conducted for the entire period that the system is visible in the night sky, pushing to much higher airmass than the LSST will use. That being said, typical time delays for four-image galaxy-scale lens systems range from a few days to several tens of days (e.g., Fassnacht et al. 2002), so a three-month observing season will be adequate for measuring delays if the lensed AGN or supernova varies such that the leading

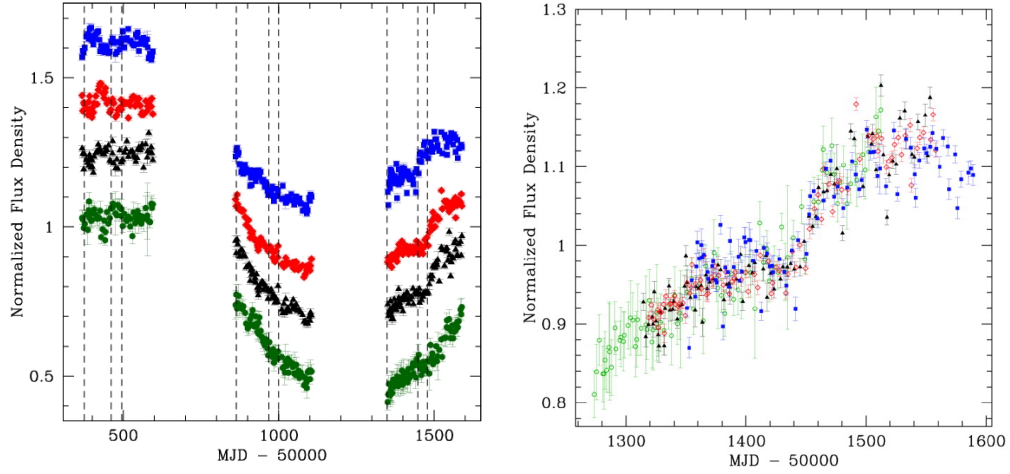


Figure 12.12: Example of time-delay measurement. *Left*: light curves of the four lensed images of B1608+656, showing three “seasons” of monitoring. The seasons are of roughly eight months in duration and measurements were obtained on average every 3 to 3.5 days. Each light curve has been normalized by its mean flux and then shifted by an arbitrary vertical amount for clarity. *Right*: the B1608+656 season 3 data, where the four images’ light curves have been shifted by the appropriate time delays and relative magnifications, and then overlaid (the symbols match those in the left panel). Figures from [Fassnacht et al. \(2002\)](#).

image variation occurs near to the beginning of the season. Ascertaining the precise effect of the season length on the number of well-measured lens systems will require some detailed simulations. This program could also be used to assess the gain in time delay precision in the 10-20% of systems that lie in the field overlap regions, and hence get observed at double cadence.

A further systematic process that can affect optical lens monitoring programs is microlensing, whereby individual stars in the lensing galaxy can change the magnification of individual lensed images. Both gradual changes, due to slow changes in the magnification pattern as stars in the lensing galaxy move, and short-scale variability, due to caustic crossings, have been observed (e.g., [Burud et al. 2002b](#); [Colley & Schild 2003](#)).

12.4.3 Moving Beyond H_0

Fundamentally a time delay in a given strong lens system measures the “time delay distance,”

$$D \equiv \frac{D_1 D_s}{D_{ls}} = \frac{\Delta t_{\text{obs}}}{f_{\text{mod}}}, \quad (12.17)$$

where D_1 and D_s are angular diameter distances to the lens (or deflector) and the source, D_{ls} is the angular diameter distance between the lens and source, and f_{mod} is a factor that must be inferred from a lens model. In individual lens systems people have used the fact that $D \propto H_0^{-1}$ to measure the Hubble constant. With a large ensemble, however, we can reinterpret the analysis as a measurement of distance (the time delay distance) versus redshift (actually both the lens and source redshifts), which opens the door to doing cosmography in direct analogy with supernovae, BAO, and the CMB.

In principle, strong lensing may be able to make a valuable contribution to cosmography because of its independence from and complementarity to these other probes. [Figure 12.13](#) illustrates this point by comparing degeneracy directions of cosmological constraints from lens time delays with those from CMB, BAO, and SNe. The lensing constraints look quite different from the others, with the notable feature that the contours are approximately horizontal — and thus particularly sensitive to the dark energy equation of state parameter w — in much of the region of interest. The value of strong lensing complementarity is preserved even when generalized to a time-dependent dark energy equation of state ([Linder 2004](#)).

In practice, of course, the challenge for strong lensing cosmography is dealing with uncertainties in the f_{mod} factor in [Equation 12.17](#). In this section we discuss an approach that involves modeling individual lenses as carefully as possible, while in [§ 12.5](#) we discuss a complementary statistical approach.

One way to minimize uncertainties in f_{mod} is to maximize the amount and quality of lens data. We will require not just image positions and time delays but also reliable (ideally spectroscopic) lens and source redshifts; we would like to have additional model constraints in the form of arc or ring images of the host galaxy surrounding the variable point source, or some other background galaxy; and we would make good use of dynamical data for the lens galaxy if available. All of this calls for follow-up observations, likely with JWST or laser guide star adaptive optics on 10-m class or larger telescopes. We expect to use the full sample of time delay lenses to select good sub-samples for such follow-up, as described in [§ 12.4.1](#).

There are systematic errors associated not just with the lens galaxy but also with the influence of mass close to the line of sight, either in the lens plane or otherwise (e.g., [Keeton & Zabludoff 2004](#); [Fassnacht et al. 2006](#); [Momcheva et al. 2006](#)). Some constraints on this “external convergence” ([§ 12.1.3](#)) can be placed by modeling all the galaxies in the field using the multi-filter photometry, and perhaps the weak lensing signal (e.g., [Nakajima et al. 2009](#)). This degeneracy between lens and environment can also be broken if we know the magnification factor itself, which is approximately true if the source is a type Ia supernova, whose light curves may be guessed a priori. The hundred or so multiply-imaged SNeIa ([Figure 12.8](#)) will be especially valuable for this time delay lens cosmography ([Oguri & Kawano 2003](#)), and may be expected to make up a significant proportion of the cosmographic strong lens sample.

12.5 Statistical Approaches to Cosmography from Lens Time Delays

Masamune Oguri, Charles R. Keeton, Phil Marshall

The large number of strong lenses discovered by LSST will permit statistical approaches to cosmography – the measurement of the distance scale of the Universe, and the fundamental parameters associated with it – that complement the detailed modeling of individual lenses. Statistical methods will be particularly powerful for two-image lenses, which often have too few lensing observables to yield strong modeling constraints, but will be so abundant in the LSST sample (see [§ 12.2](#)) that we can leverage them into valuable tools for cosmography. Note that to first order we do not

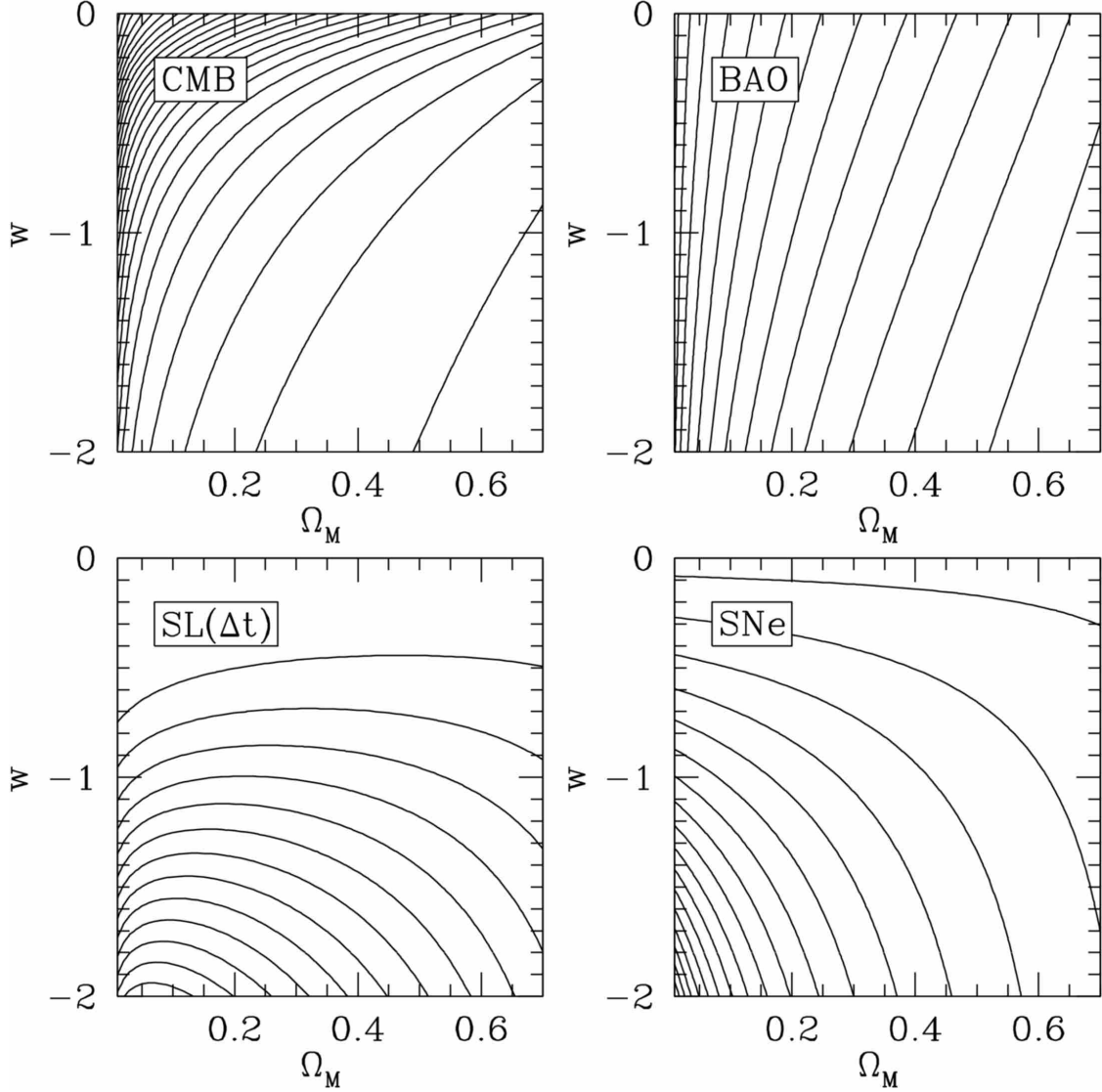


Figure 12.13: Contours of key cosmological quantities that are constrained from CMB (*upper left*), BAO (*upper right*), lensing time delay (*lower left*), and Supernovae Ia (*lower right*), which indicate the degeneracy direction from each observation. For CMB and BAO, we plot contours of $D_A(z_{\text{CMB}} = 1090)\sqrt{\Omega_M h^2}$ and $D_A(z_{\text{BAO}} = 0.35)\sqrt{\Omega_M h^2}$, respectively which are measures of the angular scale of the acoustic peak at two redshifts. For time delays, Δt , we show contours of $D \equiv D_l D_s / D_{ls}$, where we adopted $z_l = 0.5$ and $z_s = 1.8$. Contours of SNe are simply constant luminosity distance, $D_L(z_{\text{SNe}} = 0.8)$. All the contours are shown on the Ω_M - w plane, assuming a flat Universe.

need a complete sample of lenses for this measurement: we can work with any ensemble of lenses, provided we understand the form of the distributions of its members' structural parameters.

The basic idea is to construct a statistical model for the likelihood function $\Pr(\mathbf{d}|\mathbf{q}, \mathbf{p})$, where the data \mathbf{d} concisely characterize the image configurations and time delays of all detected lenses, while \mathbf{q} represents parameters related to the lens model (the density profile and shape, evolution, mass substructure, lens environment, and so on), and \mathbf{p} denotes the cosmological parameters of interest. We can then use Bayesian statistics to infer posterior probability distributions for cosmological

parameters, marginalizing over the lens model parameters \mathbf{q} (which are nuisance parameters from the standpoint of cosmography) with appropriate priors.

Here we illustrate the prospects for cosmography from statistical analysis of a few thousand time delay lenses that LSST is likely to discover. We use the statistical methods introduced by [Oguri \(2007\)](#), working with the “reduced time delay” between images i and j , $\Xi_{ij} \equiv 2c\Delta t_{ij}D_{ls}/[D_1D_s(1+z_1)(r_i^2 - r_j^2)]$, which allows us to explore how time delays depend on the “nuisance parameters” related to the lens model. Here r_i and r_j are the distances of the two images from the center of the lens galaxy. Following [Oguri \(2007\)](#), we conservatively model systematics associated with the lens model using a log-normal distribution for Ξ with dispersion $\sigma_{\log \Xi} = 0.08$. We can then combine this statistical model for Ξ with observed image positions and time delays to infer posterior probability distributions for cosmological parameters (which enter via the distances D_1 , D_s , and D_{ls}). See [Coe & Moustakas \(2009\)](#) for detailed discussions of how Ξ depends on various cosmological parameters.

From the mock catalog of lensed quasars in LSST (see § 12.2), we choose two-image lenses because they are particularly suitable for statistical analysis. We only use systems whose image separations are in the range $1'' < \Delta\theta < 3''$ and whose configurations are asymmetric with respect to the lens galaxy: specifically, we require that the asymmetry parameter $R_{ij} \equiv (r_i - r_j)/(r_i + r_j)$ be in the range $0.15 < R_{ij} < 0.8$, where Ξ is less sensitive to the complexity of lens potentials. This yields a sample of ~ 2600 lens systems. We assume positional uncertainties of $0.01''$ and time delay uncertainties of 2 days. We assume no errors associated with lens and source redshifts.

[Figure 12.14](#) shows the corresponding constraints on the dark energy equation of state, w_0 and w_a , from a Fisher matrix analysis (§ B.4.2) of the combination of CMB data (expected from Planck), supernovae (measured by a SNAP-like JDEM mission), and the strong lens time delays measured by LSST. In all cases, a flat Universe is assumed. This figure indicates that the constraint from time delays can be competitive with that from supernovae. By combining both constraints, we can achieve higher accuracy on the dark energy equation of state parameters.

One important source of systematics in this analysis is related to the (effective) slope of lens galaxy density profiles. While the mean slope only affects the derived Hubble constant, any evolution of the slope with redshift would affect other cosmological parameters as well. We anticipate that the distribution of density slopes (including possible evolution) may be calibrated by other strong lensing data (see § 12.3). In practice, this combination will have to be done carefully to avoid using the same data twice. Another important systematic error comes from uncertainties in the lens and source redshifts. The effect may be negligible if we measure all the redshifts spectroscopically as we assumed above, but this would require considerable amounts of spectroscopic follow-up observations. Instead we can use photometric redshifts for lenses and/or sources; in this case, errors on the redshifts will degrade the cosmological use of time delays (see [Coe & Moustakas 2009](#)).

12.6 Group-scale Mass Distributions, and their Evolution

Christopher D. Fassnacht

Galaxy groups are the most common galaxy environment in the local Universe (e.g., [Turner & Gott 1976](#); [Geller & Huchra 1983](#); [Eke et al. 2004](#)). They may be responsible for driving much

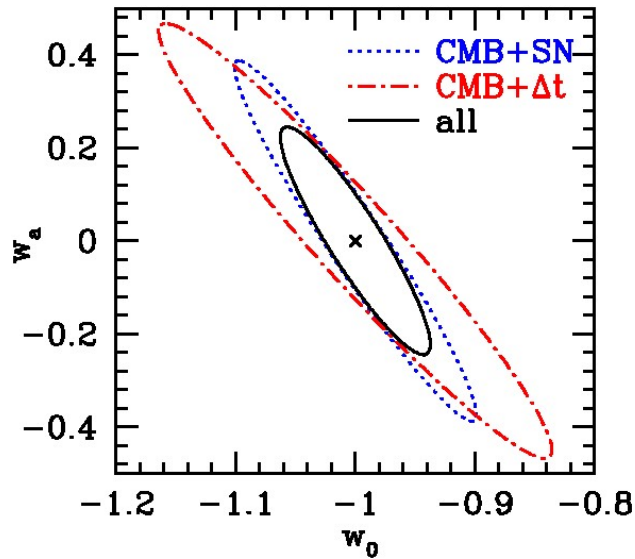


Figure 12.14: Forecast constraints on cosmological parameters in the w_0 - w_a plane, assuming a flat Universe. The CMB prior from Planck is adopted for all cases. The SN constraint represents expected constraints from a future SNAP-like JDEM mission supernova survey. Constraints from time delays in LSST are denoted by Δt .

of the evolution in galaxy morphologies and star formation rates between $z \sim 1$ and the present (e.g., Aarseth & Fall 1980; Barnes 1985; Merritt 1985), and their mass distributions represent a transition between the dark-matter dominated NFW profiles seen on cluster scales and galaxy-sized halos that are strongly affected by baryon cooling (e.g., Oguri 2006). LSST will excel in finding galaxy groups beyond the local Universe and measuring the evolution in the mass function.

Groups have been very well studied at low redshift (e.g., Zabludoff & Mulchaey 1998; Mulchaey & Zabludoff 1998; Osmond & Ponman 2004) but very little is known about moderate-redshift ($0.3 < z < 1$) groups. This is because unlike clusters they are difficult to discover beyond the local Universe. At optical wavelengths, their modest galaxy overdensities make these systems difficult to pick out against the distribution of field galaxies, while their low X-ray luminosities and cosmological dimming have confounded most X-ray searches. This situation is beginning to change with the advent of sensitive X-ray observatories such as Chandra and XMM (e.g., Willis et al. 2005; Mulchaey et al. 2006; Jeltema et al. 2006, 2007). However, the long exposure times required to make high-SNR detections of the groups have kept the sample sizes small and biased detections toward the most massive groups, i.e., those that could be classified as poor clusters. Large spectroscopic surveys are also producing samples of group candidates, although many of the candidates are selected based on only 3–5 redshifts and, thus, the numbers of false positives in the samples are large. Here, too, the sample sizes are limited by the need for intensive spectroscopic followup in order to confirm the groups and to measure their properties (e.g., Wilman et al. 2005).

Both X-ray and spectroscopic data can, in principle, be used to measure group masses. However, these mass estimates are based on assumptions about, for example, the virialization of the group, and may be highly biased. Furthermore, velocity dispersions derived from only a few redshifts of member galaxies may be poor estimators of the true dispersions (e.g., Zabludoff & Mulchaey 1998; Gal et al. 2008), further biasing dynamical mass estimates. In the case of the X-ray measurements,

even deep exposures (~ 100 ksec) may not yield high enough signal-to-noise ratios to measure spectra and, thus, determine the temperature of the intragroup gas (e.g., [Fassnacht et al. 2008](#)).

In § 12.2, we estimated that $\sim 10^3$ galaxy groups will be detected by their strong lensing alone. This will greatly advance the state of group investigations. The number of known groups beyond the local Universe will be increased by a factor of 10 or more. These groups should fall in a broad range of redshifts, including higher redshifts than those probed by X-ray-selected samples, which are typically limited to $z \leq 0.4$. More importantly, however, these lens-selected groups will all have highly precise mass measurements that are not reliant on assumptions about hydrostatic equilibrium or other conditions. Strong lensing provides the most precise method of measuring object masses beyond the local Universe, with typical uncertainties of $\sim 5\%$ or less ([Paczynski & Wambsganss 1989](#)). The combination of a wide redshift range, a large sample size, and robust mass measurements will enable unprecedented explorations of the evolution of structure in this elusive mass range.

12.7 Dark Matter (Sub)structure in Lens Galaxies

Gregory Dobler, Charles R. Keeton, Phil Marshall

Gravitationally lensed images of distant quasars ([Figure 12.15](#)) contain a wealth of information about small-scale structure in both the foreground lens galaxy and the background source. Key scales in the lens galaxy are:

- Macrolensing (~ 1 arcsec) by the global mass distribution sets the overall positions, flux ratios, and time delays of the images;
- Millilensing (~ 1 mas) by dark matter substructure perturbs the fluxes by tens of percent or more, the positions by several to tens of milli-arcseconds and the time delays by hours to days; and
- Microlensing ($\sim 1 \mu\text{as}$) by stars sweeping across the images causes the fluxes to vary on scales of months to years ([Figure 12.16](#)).

Additional scales are set by the size of the source. Broad-band optical observations measure light from the quasar accretion disk, which can be comparable in size to the Einstein radius of a star in the lens galaxy. Differences in the size of the source at different wavelengths can make microlensing chromatic (see [Figure 12.17](#) and § 12.8).

The various phenomena have distinct observational signatures that allow them to be disentangled. Time delays cause given features in the intrinsic light curve of the source to appear in all the lensed images but offset in time; so they can be found by cross-correlating image light curves. Microlensing causes uncorrelated, chromatic variations in the images; so it is revealed by residuals in the delay-corrected light curves. Millilensing leads to image fluxes, positions, and time delays that cannot be explained by smooth lens models; it can always be identified via lens modeling, and in certain four-image configurations the detection can be made model-independent ([Keeton et al. 2003, 2005](#)).

The key to all this work is having the well-sampled, six-band light curves provided by LSST. The planned cadences should make it possible to determine the time delays of most two-image lenses,

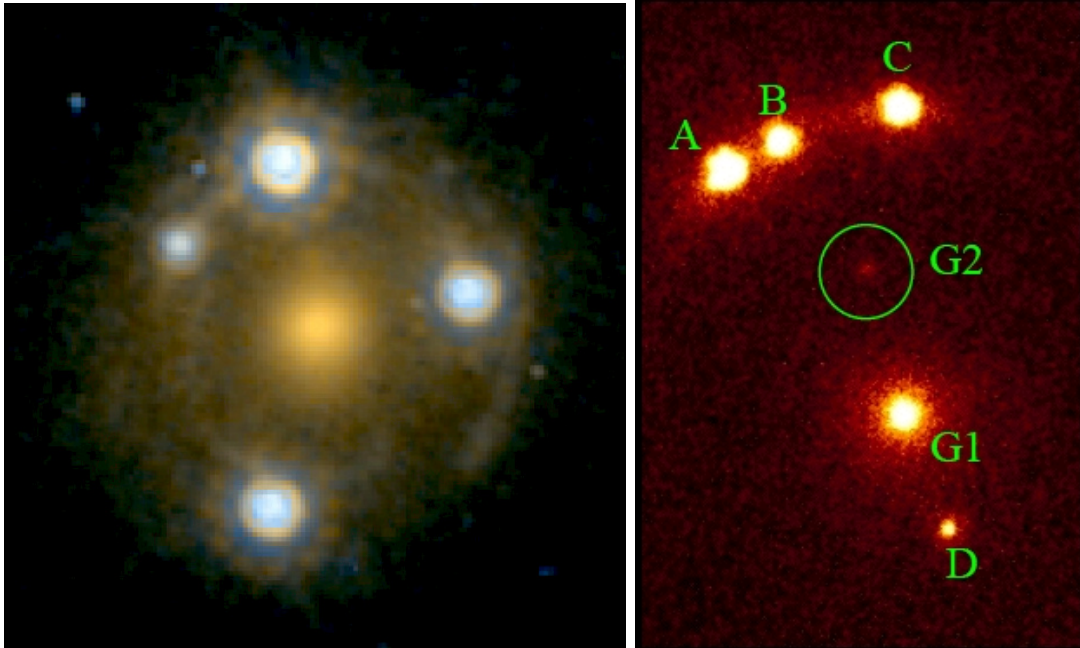


Figure 12.15: Two of the most extreme “flux ratio anomalies” in four-image lenses. *Left*: HST image of SDSS J0924+0219 (from Keeton et al. 2006). A quasar at redshift $z_s = 1.52$ is lensed by a galaxy at $z_l = 0.39$ into four images, which lie about $0.9''$ from the center of the galaxy. Microlensing demagnifies the image at the top left by a factor > 10 , relative to a smooth mass distribution. *Right*: Keck adaptive optics image of B2045+265 (from McKean et al. 2007) showing the lensing galaxy (G1) and four lensed images of the background AGN (A–D). Smooth models predict that image B should be the brightest of the three close lensed images, but instead it is the faintest, suggesting the presence of a small-scale perturbing mass. The adaptive optics imaging reveals the presence of a small satellite galaxy (G2) that may be responsible for the anomaly.

and multiple time delays in many four-image lenses. The multicolor light curves will have more than enough coverage to extract microlensing light curves, which will not only enable their own science but also reveal the microlensing-corrected flux ratios that can be used to search for CDM substructure (§ 12.7.1).

In this section we discuss using milli- and microlensing to probe the distribution of dark matter in lens galaxies on sub-galactic scales. In § 12.8 and § 10.7 we discuss using microlensing to probe the structure of the accretion disks in the source AGN.

12.7.1 Millilensing and CDM Substructure

Standard lens models often fail to reproduce the fluxes of multiply-imaged point sources, sometimes by factors of order unity or more (see Figure 12.15). In many cases these “flux ratio anomalies” are believed to be caused by subhalos in the lens galaxy with masses in the range $\sim 10^6$ – $10^{10} M_\odot$. CDM simulations predict that galaxy dark matter halos should contain many such subhalos that are nearly or completely dark (for some recent examples, see Diemand et al. 2008; Springel et al. 2008). Strong lensing provides a unique opportunity to detect mass clumps and thus test CDM predictions, probe galaxy formation on small scales, and obtain astrophysical evidence about the nature of dark matter (e.g., Metcalf & Madau 2001; Chiba 2002).

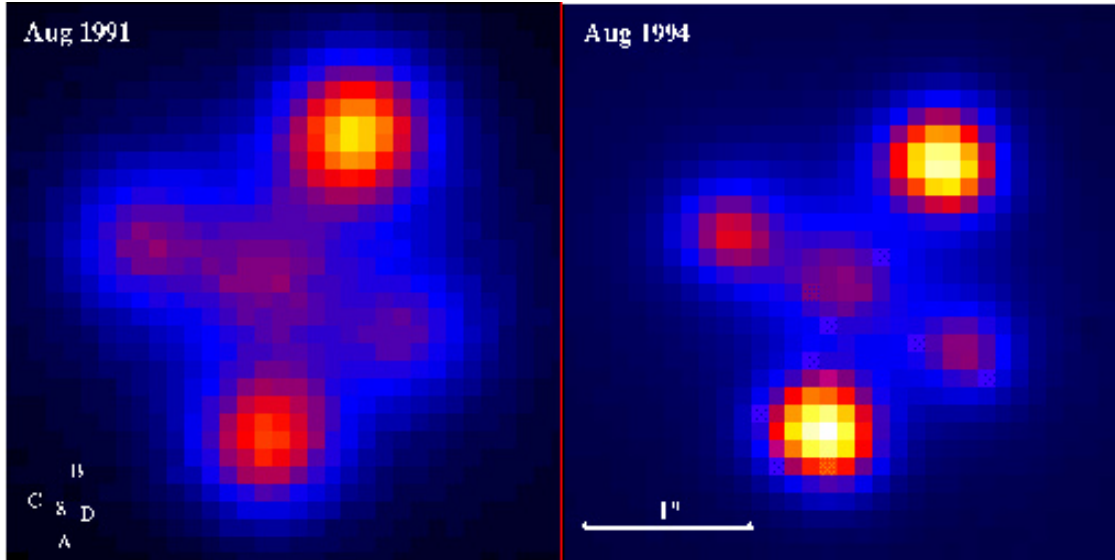


Figure 12.16: Microlensing-induced variability in the “Einstein Cross” lens Q2237+0305, from Lewis, Irwin, et al., <http://apod.nasa.gov/apod/ap961215.html>. The relative fluxes in the four images are noticeably different in images taken three years apart.

The LSST lens sample should be large enough to allow us to probe the mass fraction contained in substructure, its evolution with redshift, the mass function and spatial distribution of subhalos within parent halos, and the internal density profiles of the subhalos. LSST monitoring of the lenses will be essential to remove flux perturbations from smaller objects in the lens galaxy, namely microlensing by stars. This will enable us to expand millilensing studies from the handful of four-image radio lenses available today to a sample of well-monitored optical lenses that is some two orders of magnitude larger.

Flux Ratio Statistics

Millilensing by CDM substructure is detected not through variability (the time scales are too long) but rather through observations of image flux ratios, positions, and time delays that cannot be produced by any reasonable smooth mass distribution. Flux ratio anomalies consistent with CDM substructure have already been observed in a small sample of four-image lenses; they provide the only existing measurement of the amount of substructure in galaxies outside the Local Group (Dalal & Kochanek 2002).

Presently, constraints on substructure in distant galaxies are limited by sample size because the analysis has been restricted to four-image radio lenses. Four-image lenses have been the main focus for millilensing studies because they provide many more constraints than two-image lenses, and that will continue to be the case with LSST. Radio flux ratios have been required to date because optical flux ratios are too contaminated by stellar microlensing (only at radio wavelengths is the source large enough to be insensitive to stars). The breakthrough with LSST will come from exploiting the time domain information to measure microlensing well enough to remove its effects and uncover the corrected flux ratios. In this way LSST will finally make it possible to use optical

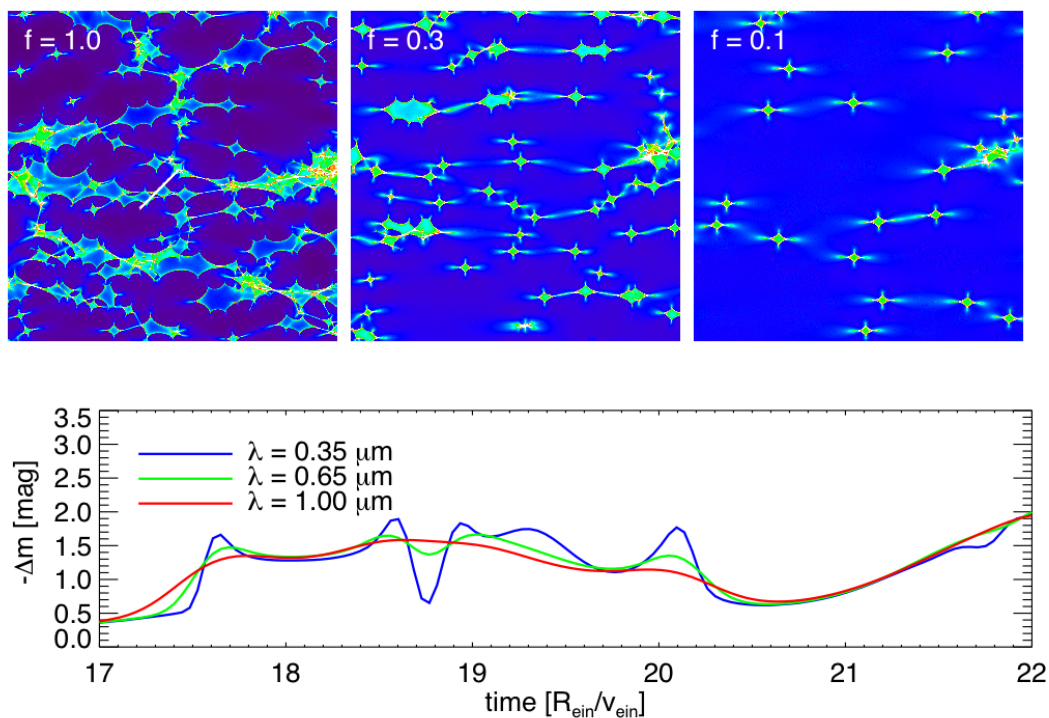


Figure 12.17: The maps in the top panels show examples of the lensing magnification for a very small patch of the source plane just $30R_E$ cm on a side, where $R_E \sim 5 \times 10^{16}$ cm is the Einstein radius of a single star in the lens galaxy. The panels have the same total surface mass density but a different fraction f^* of mass in stars (the remaining mass is smoothly distributed). The magnification varies over micro-arcsecond scales due to light bending by individual stars. As the background source moves relative to the stars (as shown by the white line in the upper left panel), it feels the changing magnification leading to variability in the light curves as shown in the bottom panel. The variability amplitude depends on wavelength because AGN have different effective sizes at different wavelengths (see § 12.8). From Keeton et al. (2009).

flux ratios to study CDM substructure. The data volume will increase the sample of four-image lenses available for millilensing by some two orders of magnitude.

The statistics of flux ratio anomalies reveal the overall abundance of substructure (traditionally quoted as the fraction of the projected surface mass density bound in subhalos), followed by the internal density profile of the subhalos (Shin & Evans 2008). These lensing measurements are unique because most of the subhalos are probably too faint to image directly. With the large sample provided by LSST, it will be possible to search for evolution in CDM substructure with redshift (see below).

Time Delay Perturbations

In addition to providing flux ratios, LSST will open the door to using time delays as a new probe of CDM substructure. Figure 12.18 shows an example of how time delays are perturbed by CDM subhalos. The perturbations could be detected either as residuals from smooth model fits (Keeton & Moustakas 2009) or as inconsistencies with broad families of smooth models (Congdon et al.

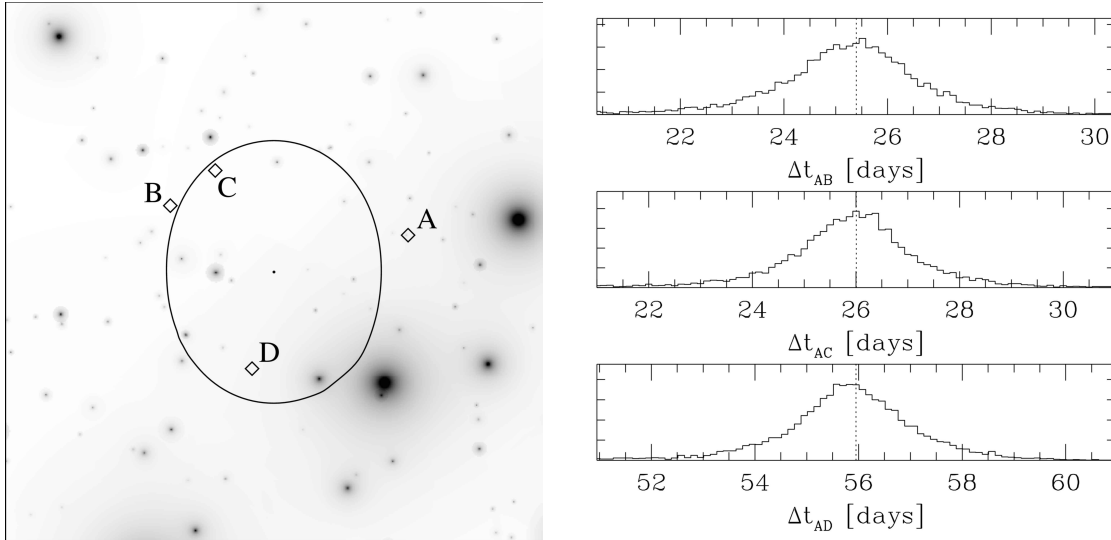


Figure 12.18: *Left*: sample mass map of CDM substructure (after subtracting away the smooth halo) from semi-analytic models by [Zentner & Bullock \(2003\)](#). The points indicate example lensed image positions, and the critical curve is shown. *Right*: histograms of the time delays between the images, for 10^4 Monte Carlo simulations of the substructure (random positions and masses). The dotted lines show what the time delays would be if all the mass were smoothly distributed. (Figures from [Keeton 2009b](#))

[2009](#)). Time delays are complementary to flux ratios because they probe a different moment of the mass function of CDM subhalos, which is sensitive to the physical properties of the dark matter particle. Also, time delay perturbations are sensitive to the entire population of subhalos in a galaxy, whereas flux ratios are mainly sensitive to subhalos projected in the vicinity of the lensed images ([Keeton 2009a](#)).

The number of LSST lenses with time delays accurate enough ($\lesssim 1$ day) to constrain CDM substructure will depend on the cadence distribution and remains to be determined. It is clear, though, that LSST will provide the first large sample of time delays, which will enable qualitatively new substructure constraints that provide indirect but important astrophysical evidence about the nature of dark matter.

The Evolution of CDM Substructure

The lens galaxies and source quasars LSST discovers will span a wide range of redshift, and hence cosmic time (§ 12.2). The sample will be large enough that we can search for any change in the amount of CDM substructure with redshift/time. Determining whether the amount of CDM substructure increases or decreases with time will reveal whether the accretion of new subhalos or the tidal disruption of old subhalos drives the abundance of substructure. Also, the cosmic evolution of substructure is a key prediction of dark matter theories that is not tested any other way.

12.7.2 Microlensing Densitometry

It is not surprising that the amplitude and frequency of microlensing fluctuations are sensitive to the density of stars in the vicinity of the lensed images. What may be less obvious is that microlensing is sensitive to the density of smoothly distributed (i.e., dark) matter as well. The reason is twofold: first, the global properties of the lens basically fix the *total* surface mass density at the image positions, so decreasing the surface density in stars must be compensated by increasing the surface density in dark matter; second, there are nonlinearities in microlensing such that the smooth matter can actually enhance the effects of the stars (Schechter & Wambsganss 2002). These effects are illustrated in Figure 12.17.

The upshot is that measuring microlensing fluctuations can reveal the relative densities of stars and dark matter at the positions of the images. This makes microlensing a unique tool for measuring *local densities* (as opposed to integrated masses) of dark matter in distant galaxies. The large LSST sample of microlensing light curves will make it possible to measure stellar and dark matter densities as a function of both galactic radius and redshift.

12.8 Accretion Disk Structure from 4000 Microlensed AGN

George Chartas, Charles R. Keeton, Gregory Dobler

Microlensing by stars in the lens galaxy creates independent variability in the different lensed images. With a long, high-precision monitoring campaign, the microlensing variations can be disentangled from intrinsic variations of the source. While light bending is intrinsically achromatic, color effects can enter if the effective source size varies with wavelength (see Figure 12.17). Chromatic variability is indeed observed in lensed AGN, indicating that the effective size of the emission region – the accretion disk – varies with wavelength. This effect can be used to probe the temperature profile of distant accretion disks on micro-arcsecond scales. The LSST sample will be two orders of magnitude larger than the lensed systems currently known, so we can study accretion disk structure as function of AGN luminosity, black hole mass, and host galaxy properties.

This is a joint project with the AGN science collaboration. § 10.7 contains the AGN science case; here we discuss very briefly the microlensing physics.

Quasar Accretion Disks under a Gravitational Microscope

Individual stars in a lens galaxy cause the lensing magnification to vary across micro-arcsecond scales. As the quasar and stars move, the image of the accretion disk responds to the changing magnification, leading to variability that typically spans months to years but can be more rapid when the source crosses a lensing caustic. We show typical microlensing source-plane magnification maps in Figure 12.17; the caustics are the bright bands. The variability amplitude depends on the quasar size relative to the Einstein radius of a star (projected into the source plane), which is

$$R_E \sim 5 \times 10^{16} \text{ cm} \times \left(\frac{m}{M_\odot} \right)^{1/2} \quad (12.18)$$

for typical redshifts. According to thin accretion disk theory, the effective size of the thermal emission region at wavelength λ is

$$R_\lambda \simeq 9.7 \times 10^{15} \text{cm} \times \left(\frac{\lambda}{\mu\text{m}} \right)^{4/3} \left(\frac{M_{\text{BH}}}{10^9 M_\odot} \right)^{2/3} \left(\frac{L}{\eta L_{\text{Edd}}} \right)^{1/3}, \quad (12.19)$$

where η is the accretion efficiency. By comparing the variability amplitudes at different wavelengths, we can determine the relative source sizes and test the predicted wavelength scaling. With black hole masses estimated independently from emission line widths, we can also test the mass scaling. These methods are in use today (e.g., Kochanek et al. 2006a), but the expense of dedicated monitoring has limited sample sizes to a few.

12.9 The Dust Content of Lens Galaxies

Árdís Elíasdóttir, Emilio E. Falco

The interstellar medium (ISM) in galaxies causes the extinction of light passing through it, with the dust particles scattering and absorbing the incoming light and re-radiating them as thermal emission. The resulting extinction curve, i.e., the amount of dust extinction as a function of wavelength, is dependent on the composition, amount, and grain size distribution of the interstellar dust. Therefore, extinction curves provide important insight into the dust properties of galaxies.

Probing dust extinction at high redshift is a challenging task: the traditional method of comparing lines of sight to two standard stars is not applicable, since individual stars cannot be resolved in distant galaxies. Various methods have been proposed to measure extinction at high redshift, including analysis of SNe curves (Riess et al. 1998; Perlmutter et al. 1997; Riess et al. 1996; Krisciunas et al. 2000; Wang et al. 2006), gamma-ray burst light curves (Jakobsson et al. 2004; Elíasdóttir et al. 2008), comparing reddened (i.e., dusty) quasars to standard quasars (see e.g., Pei et al. 1991; Murphy & Liske 2004; Hopkins et al. 2004; Ellison et al. 2005; York et al. 2006; Malhotra 1997), and lensed quasars.

Gravitationally lensed multiply imaged background sources provide two or four sight-lines through the deflecting galaxy (see Figure 12.1), allowing the differential extinction curve of the intervening galaxy to be deduced. This method has already been successfully applied to the current, rather small, sample of multiply imaged quasars (see e.g., Falco et al. 1999; Wucknitz et al. 2003; Muñoz et al. 2004; Wisotzki et al. 2004; Goicoechea et al. 2005; Elíasdóttir et al. 2006).

As discussed in § 12.2, it is expected that the LSST will discover several thousand gravitationally lensed quasars with lens galaxy redshifts ranging from 0–2. In addition, around 300 gravitationally lensed SNe are expected to be found. This combined sample will allow us to conduct statistical studies of the extinction properties of high redshift galaxies and the evolution of those dust distributions with redshift. Furthermore, it will be possible to determine the differences in the extinction properties as a function of galaxy type. Although lensing galaxies are predominantly early-type, we expect that 20–30% may be late-type. The study of dust extinction properties of spiral galaxies will be especially relevant for SNe studies probing dark energy, as dust correction could be one of the major sources of systematic error in the analysis. The lensing sample will provide an independent and complementary estimate of the dust extinction for use in these surveys. All these studies

will be possible as a function of radius from the center of the lensing galaxy, since the images of lensed quasars typically probe lines of sight at different radii.

One of the major strengths of the LSST survey is that it will monitor all lens systems over a long period, making it possible to correct for contamination from both microlensing and intrinsic variation in the background object. In addition, for the lensed SNe, once the background source has faded, it will be possible to do a followup study of the dust emission in the lensing galaxy. This will make it possible for the first time to do a comparative study of dust extinction and dust emission in galaxies outside the Local Group.

12.9.1 Lens Galaxy Differential Extinction Curves with the LSST

The LSST sample will yield extinction curves from the ultraviolet to the infrared; different regions of the extinction curve will be sampled in different redshift bins. The infrared slope of extinction curves will be best constrained by the lower-redshift systems, whereas the UV slope will be best constrained by the higher-redshift systems. One of the most prominent features of the Milky Way extinction curve, a “bump” at about 2200 Å of excess extinction, possibly due to polycyclic aromatic hydrocarbons (PAHs), will be probed by any system at a redshift of $z_1 \gtrsim 0.4$.

It is important to keep in mind that the derived extinction curves will be *differential* extinction curves and not absolute ones, except in the limit where one line of sight is negligibly extinguished compared to the other. Therefore, the derived total amount of extinction (e.g., scaled to the V-band, A_V), is always going to be a lower bound on the absolute extinction for the more extinguished line of sight.

The differential extinction law is of the same type for both linear (Small Magellanic Cloud, SMC) and Milky Way (MW) extinction laws. Defining $R_V \equiv A_V/E$, where the reddening $E = E(B - V)$ between the B and V bands is given by $E \equiv A_B - A_V$, we can write the differential extinction between images A and B for MW dust as (for details, see [Elíasdóttir et al. 2006](#)):

$$\begin{aligned} \frac{R_V^{\text{diff}}}{R_V^{\text{B}}} &= \frac{E^{\text{B}} - E^{\text{A}} R_V^{\text{A}}/R_V^{\text{B}}}{E^{\text{B}} - E^{\text{A}}} \\ &= 1 + \frac{E^{\text{A}}}{E^{\text{B}} - E^{\text{A}}} \left(1 - \frac{R_V^{\text{A}}}{R_V^{\text{B}}}\right) \\ &\equiv 1 + \eta. \end{aligned} \tag{12.20}$$

This says that the error due to the non-zero extinction of image A that is introduced when using R_V^{diff} as an estimator for R_V is

$$\eta = \frac{E^{\text{A}}/E^{\text{B}}}{1 - E^{\text{A}}/E^{\text{B}}} \left(1 - \frac{R_V^{\text{A}}}{R_V^{\text{B}}}\right). \tag{12.21}$$

A biased estimate will only arise if either the amount of extinction along the two lines of sight is very similar, or if the type of extinction along the two lines of sight is very different (see [Figure 12.19](#)). In the first case, the measured differential extinction will, however, be close to zero, so these systems can be automatically excluded from the sample. In the second case, we must consider how much

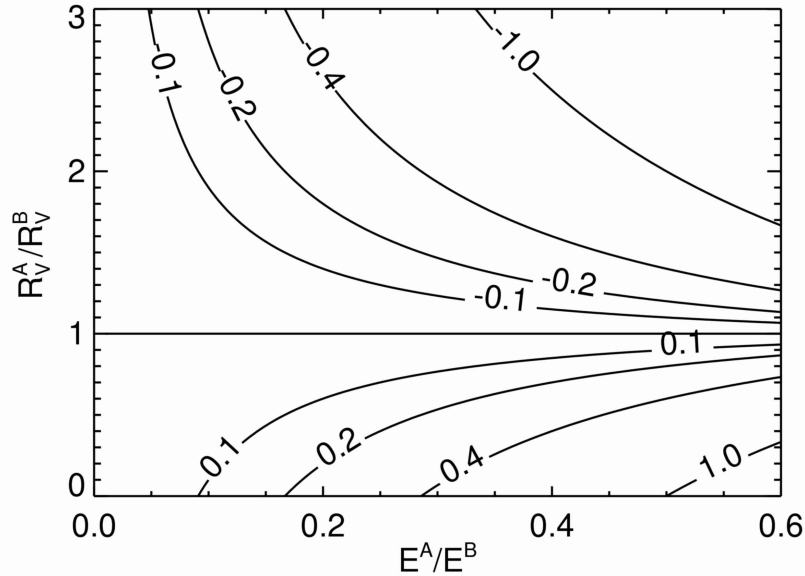


Figure 12.19: A contour plot showing the bias in the derived value of R_V^{diff} due to extinction along both lines of sight. The bias is negligible if the extinction along one line of sight dominates the other or if the R_V 's along the two lines of sight are similar. Figure taken from [Elíasdóttir et al. \(2006\)](#).

the extinction law might vary within a given galaxy. For SMC, LMC and MW dust most lines of sight have very similar values of R_V , but outliers do exist. For example, if we take the most extreme values of the Milky Way we need $E^A/(E^B - E^A) \leq 0.05$ for reaching a 10% accuracy in R_V .

12.9.2 Dealing with Microlensing and Intrinsic Variations

While lensing is in general achromatic, microlensing can resolve color gradients in accretion disks (§ 12.8), therefore can cause a color variation which may mimic dust extinction. Microlensing typically causes changes in brightness $\lesssim 1$ mag, and the chromatic variation is typically $\lesssim 10\%$, so for strongly extinguished systems this effect is expected to be minor (see e.g., [Mosquera et al. 2008](#)). However, as LSST will monitor the lenses over long time spans, independent estimates of the potential microlensing bias will be obtained, and a correction can be made if necessary. Likewise, the intrinsic (and chromatic) variability of the AGN can be corrected for, provided the lens time delay between images is known. The long-term monitoring will be essential for this: how well the time delayed intrinsic variations can be removed with three-month monitoring seasons is to be demonstrated.

12.9.3 Follow-up Observations

It would be desirable to obtain X-ray measurements for at least a subsample of the gravitationally lensed systems studied in this survey (see e.g., [Dai & Kochanek 2008](#)). In the case where dust

extinction is detected, an X-ray measurement can provide the neutral hydrogen column density along the two (or four) image sight-lines. This can be used to check the reliability that one line of sight is significantly less extinguished than the other and to estimate the dust-to-gas ratio. Also, one can get an estimate of how many of the “zero differential extinction” systems contain dust and how many of them are truly dust free. An X-ray telescope with a resolution of the order of $\sim 1''$ will be required for such a followup to resolve the different lines of sight. Chandra could easily be used if still in operation, while the planned resolution for the International X-ray Observatory (IXO) would limit the study to large separation lenses.

In the case of the multiply imaged SNe, a deep study of the lensing galaxies can be obtained once the SNe have faded. The PAHs thought to give rise to the bump in the MW extinction curve have characteristic emission lines in the infrared which can be measured to give an estimate on the PAH abundance (see e.g., [Draine et al. 2007](#)). With the lensing information about the type of dust extinction, it would be possible to correlate the strength of the bump to the PAH abundance. If the bump is due to the PAHs, a strong correlation should be seen.

12.9.4 Technical Feasibility

LSST data are expected to have ample sensitivity and dynamic range to yield a sample of lensed quasars with measured extinction curves up to two orders of magnitude larger than the existing one. Clear requirements for extracting high-quality extinction curves are broad wavelength coverage, seeing consistently below 1 arcsec, and stable and consistent PSFs. The high resolution and broad wavelength coverage make the LSST data set ideal for such a dust study while the frequent sampling with a consistent set of filters will be crucial to address the systematic effects of microlensing and time delays. While PS1 and DES are expected to yield similar data sets, they lack the frequent sampling required to deal with these systematic effects.

A reasonably accurate redshift for the lensing galaxy is also required to calibrate the extinction curves and to reliably search for the excess extinction around 2200 \AA . The photometric redshifts from the LSST should be sufficient: an uncertainty of $0.04(1+z)$ per galaxy (§ 3.8.4) in the photometric redshift translates to an $\sim 150 \text{ \AA}$ uncertainty in the center of the bump for a lensing galaxy at $z \sim 0.8$, which is smaller than the typical width of the bump.

The PAH abundance study will require additional follow-up observations of selected systems in the infrared. The PAH emission features range from $3\text{--}11 \mu\text{m}$ in the rest-frame which will correspond to a range of $7\text{--}23 \mu\text{m}$ for redshifts of $z = 1.0$. The planned MIRI spectrograph on the JWST has imaging capabilities and a spectrograph capable of covering this range with a sensitivity far superior to that of current facilities.

12.10 Dark Matter Properties from Merging Cluster Lenses

Maruša Bradač, Phil Marshall, Anthony Tyson

Clusters of galaxies are composed of large amounts of dark matter. These clusters are unique in their power to directly probe and place limits on the self-interaction cross-section of dark matter ([Clowe et al. 2006](#); [Bradač et al. 2006, 2008a](#)). Furthermore, in clusters we can probe the spatial

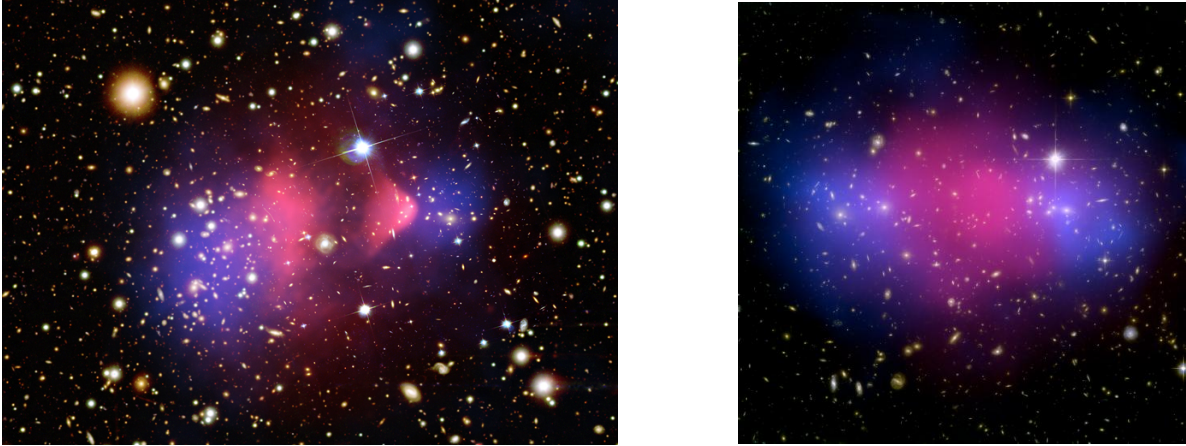


Figure 12.20: The color composite of the Bullet cluster 1E0657–56 (*left*) and MACS J0025.4–1222 (*right*). Overlaid in *blue* shade is the surface mass density map from the weak lensing mass reconstruction. The X-ray emitting plasma is shown in *red*. Both images subtend ~ 10 arcmin on the vertical axis. Credit (*left*): X-ray NASA/CXC/CfA Optical: NASA/STScI; Magellan/U.Arizona; Clowe et al. (2006); Bradač et al. (2006) (*right*) X-ray (NASA/CXC/Stanford/S.Allen); Optical/Lensing (NASA/STScI/UCSB/M.Bradač); Bradač et al. (2008b).

distribution of dark matter and its interplay with the baryonic mass component (e.g., as shown with RXJ1345–1145; Bradač et al. 2008b), and thereby study effectively the formation and evolution of clusters, one of the more robust predictions of currently favored Λ CDM cosmologies.

12.10.1 Merging Galaxy Clusters as Dark Matter Laboratories

The standard Cold Dark Matter model makes definite predictions for the characteristics of dark matter halos, including their inner slopes and concentrations. These predictions have not been tested accurately yet. Massive clusters are the best places we know for doing so; the dark matter distribution in clusters even has the potential of constraining the interaction cross-sections of the dark matter particles themselves.

The most striking examples of such investigations to date have been the Bullet cluster 1E0657–56 (Clowe et al. 2006; Bradač et al. 2006) and MACS J0025.4–1222 (Bradač et al. 2008a). These are examples of merging or colliding clusters, where the interaction has happened in the plane of the sky; the (almost) collisionless dark matter and galaxies have ended up with different, more widely-separated distributions than the collisional X-ray emitting gas, which remains closer to the interaction point. In these systems, the positions of the gravitational potential wells and the dominant baryonic component are well separated, leading us to infer the clear presence and domination of a dark matter mass component (see Figure 12.20). A union of the strong lensing data (information from highly distorted arcs) and weak lensing data (weakly distorted background galaxies) for the cluster mass reconstruction has been demonstrated to be very successful in providing a high-fidelity, high signal-to-noise ratio mass reconstruction over a large area (Bradač et al. 2006, 2008a). It was this gravitational lensing analysis that first allowed the presence of dark matter to be confirmed, and then limits on the self-interaction cross-section of dark matter particles to be estimated. The latter are currently at $\sigma/m < 0.7 \text{ cm}^2 \text{ g}^{-1}$ (Randall et al. 2008). LSST can act as a

finder for more massive, merging systems, and allow accurate lensing measurements of the relative positions of the stellar and dark matter distributions.

12.10.2 Breaking Degeneracies with Multiple Data Sets

Merging clusters are, however, not the only places where dark matter can be studied. It was first proposed by Navarro et al. (1997) that the dark matter halos on a variety of scales should follow a universal profile (the so-called Navarro Frenk and White or NFW profile) within the currently accepted Λ CDM paradigm. The three-dimensional density distribution of dark matter should follow $\rho_{\text{DM}} \propto r^{-1}$ within a scale radius r_s and fall off more steeply at radii beyond that ($\rho_{\text{DM}} \propto r^{-3}$). In practice, however, the density profiles of simulated clusters appear to be less concentrated and often at odds with gravitational lensing observations (Limousin et al. 2007; Broadhurst et al. 2005; Sand et al. 2008). A central baryon enhancement that could explain these discrepancies is not observed, leaving us with a puzzle. However, now for the first time supercomputers and simulations have become powerful enough to give clear predictions of not only the distribution and amounts of dark matter, but also its interplay with the baryons and the effects the baryons have on the formation of dark matter halos (e.g., through adiabatic contraction, Gnedin et al. 2004; Nagai et al. 2007).

It is, therefore, high time that the predictions of simulations are paired with state-of-the-art observations of evolving clusters. A high-resolution, absolutely-calibrated mass map of galaxy clusters in various stages of evolution at all radii will allow us to measure the slopes of dark matter and baryonic profiles, which are a critical test of cosmology and a key to understanding the complicated baryonic physics in galaxy clusters. Several works have previously studied mass distributions in number of clusters using combined strong (information from highly distorted arcs) and weak (weakly distorted background galaxies) lensing reconstruction (see e.g., Bradač et al. 2006, 2008b; Natarajan & Kneib 1996; Kneib et al. 2003; Marshall et al. 2002; Diego et al. 2005; Jee et al. 2007; Limousin et al. 2007) and combined strong lensing and stellar kinematics data of the dominating central galaxy (Sand et al. 2008). These approaches offer valuable constraints for determining the mass distributions. At present, results range from consistent to inconsistent with Λ CDM (Bradač et al. 2008b; Sand et al. 2008; Medezinski et al. 2009, see also Figure 12.23). However, these studies all lack either a sophisticated treatment of baryons or a self-consistent combination of data on either large (around the virial radius) or small scales (around the core radius). It is, therefore, crucial to use a combination of weak and strong lensing data, matched with the method allowing mass reconstruction in the full desired range, from the inner core (~ 100 kpc) to the outskirts ($\gtrsim 1000$ kpc), with accuracy in total mass estimates of $\lesssim 10\%$, and proper account of baryons.

12.10.3 A Kilo-cluster Sample with LSST

LSST will be well-placed to support this project, since it combines multi-color high-resolution imaging over a large field of view. This will allow us to detect clusters in two different ways: by optical and photometric redshift overdensity and by weak lensing shear strength. We can expect the LSST massive cluster sample to number in the thousands (§ 12.2, § 14.3.7), with the fraction of clusters showing strong lensing effects increasing to unity at the high mass end.

Once found, the high quality cluster images will permit the identification of large numbers of strongly lensed multiple imaged systems, as well as allow us to perform weak lensing measurements all the way out to the virial radius ($\gtrsim 1000$ kpc). One significant technical challenge will be to automate the multiple image system identification procedure: currently, each individual cluster is analyzed in great detail, with a mass model being gradually built up as more and more systems are visually identified.

The statistical uncertainties in the measured photometric redshifts of these systems will be more than adequate for this project. The “catastrophic outliers” do not pose a significant problem, since the geometry of lensing is redshift-dependent, allowing us to distinguish a low from high-redshift solution. The spectroscopic follow-up is therefore not crucial, however it eases the analysis considerably, increases the precision, and can be achieved with a moderate/high investment (300 nights on a 10-m class telescope for a total of 1000 clusters).

To study the influence of baryons, auxiliary X-ray data to study the gas distribution in the clusters will be needed. Many clusters already have such data available (typically one needs 20 ks exposures with Chandra for a $z \sim 0.3$ cluster), and we expect many more to be covered with current and future X-ray surveys. To probe dark matter properties with merging clusters, an additional requirement will be a deeper X-ray follow up. These follow-ups are currently already possible with Chandra and since the sample for this part of the study is much smaller (10-100), we expect to be able to use future X-ray missions to achieve this goal.

With a sample of $\gtrsim 1000$ clusters capable of strong lensing paired with accurate mass reconstruction from the very center to the outskirts, LSST will be able to achieve a number of interesting science goals:

1. Clusters of galaxies are unique in their power to directly probe and place limits on the self-interaction cross-section of dark matter. With a subsample of clusters that are merging clusters (10 – 100 out of ~ 1000 capable of strong lensing), these limits can be significantly improved and systematic errors inherent to studies of single clusters (1E0657–56, MACSJ0025-1222) can be reduced to negligible amounts.
2. Studying the distribution of dark matter in $\gtrsim 1000$ clusters of galaxies will allow us to follow the growth of dark matter structure through cosmic time, including its interplay with the baryonic mass component, thereby allowing us to effectively study cluster formation and evolution and test a scenario which is one of the more robust predictions of currently favored Λ CDM cosmology. Examples of CDM-predicted quantities that can be probed are the profile concentration (and its relation to halo mass and redshift), halo ellipticity, and substructure mass function.
3. Well-calibrated clusters can also be used as cosmic telescopes (see § 12.11), thereby enabling the study of intrinsically lower luminosity galaxies than would otherwise be observable with even the largest telescopes.

12.11 LSST’s Giant Array of Cosmic Telescopes

Maruša Bradač, Phil Marshall

What are the sources responsible for cosmic reionization? The most efficient way to study galaxy populations shortly after the reionization epoch is to use clusters of galaxies as gravitational telescopes. With a cluster-scale gravitational lens one can gain several magnitudes of magnification, enabling the study of intrinsically lower luminosity galaxies than would otherwise be observable with even the largest telescopes (e.g., Ellis et al. 2001; Richard et al. 2006; Hu et al. 2002). With a sample of well-chosen clusters (to achieve the best efficiency and to beat the cosmic variance) the properties of these first galaxies can be determined, enabling us to address the question of whether these objects were responsible for reionizing the Universe. Furthermore, gravitational lensing is very efficient in rejecting possible interlopers (cool stars, $z \approx 2$ old galaxies) that plague such surveys in the field environment.

12.11.1 Galaxy Clusters as Tools to Explore Reionization

Theoretical studies suggest that the Universe underwent a transition from highly neutral to a highly ionized state in a relatively short period (“reionization”) at $z > 6$ (Dunkley et al. 2008). It is thought that $z > 6$ proto-galaxies were responsible for this process. However, the luminosity function of $z \gtrsim 7$ objects is quite uncertain (e.g., Stanway et al. 2008; Henry et al. 2007; Stark et al. 2007; Bouwens et al. 2008), as is their role in reionization. If these objects did indeed reionize the Universe, non-standard properties (such as unusually high abundance of faint sources, large stellar masses, and/or very low metallicities) may need to be invoked. These results are based on tiny samples ($\lesssim 10$) and so need to be confirmed with larger samples across different patches of sky in order to beat the sample variance. Finding more sources at the highest redshifts is therefore crucial. Observations at these high redshifts are extremely challenging, not only due to the large luminosity distance to these objects, but also due to their intrinsically low luminosity (stemming from their presumably lower stellar masses compared to moderate redshifts).

12.11.2 Observational Issues

One can find high redshift galaxies by searching for the redshifted Lyman break using broad-band photometry (§ 9.7. $z \simeq 6$ objects will not be detected at i and blueward, and $z \simeq 7-8$ will be z -band dropouts (e.g., Henry et al. 2007; Stanway et al. 2008; Bouwens et al. 2008). The main limitations of experiments to look for such objects to date have been the small fields examined and the difficulty of spectroscopic confirmation.

Both these observational issues can, however, be addressed when using galaxy clusters as *gravitational telescopes*. This technique was proposed shortly after the discovery of the first arcs in galaxy clusters (Soucail 1990) and has been consistently delivering record holders in the quest for the search for high redshift galaxies (Kneib et al. 2004; Bradley et al. 2008, see also Figure 12.21a,b): the brightest objects of a given class are often, if not always lensed. This is of course also the case at “lower” ($z \sim 3$) redshifts, some of the examples are the “Cosmic Eye” (Smail et al. 2007) and the bright sub-mm galaxy behind the Bullet Cluster (Gonzalez et al. 2009; Wilson et al. 2008, see also Figure 12.21c,d). The magnification effect provided by the deep gravitational potential well of a massive cluster allows detections of objects more than a magnitude fainter than the observation limit. Hence, clusters of galaxies offer the best opportunity to study the faintest, smallest and most

distant galaxies in the Universe. Due to this magnification, the solid angle of the search area effectively decreases — but since the luminosity function is practically exponential at the magnitudes one needs to probe, we can make substantial gains using the lensing magnification. In addition, these sources are observed with increased spatial resolution. As a result, we can resolve smaller physical scales than would otherwise be possible, and begin to actually measure the properties of $z \gtrsim 7$ galaxies on an individual basis.

Searches for $z \gtrsim 7$ objects in the field are plagued by the fact that, based on optical and IR colors alone, it is very difficult to distinguish between $z \gtrsim 7$ objects, old and dusty elliptical galaxies (the 4000 Å break at $z \approx 2$ can potentially be mistaken for a Lyman break at $z > 7$), and cool T and L-dwarf stars (see e.g., [Stanway et al. 2008](#)). As shown by these authors, Spitzer/IRAC data can help to exclude some, but not all, of the interlopers. Gravitational lensing alleviates all these problems if the objects observed are multiply imaged. Since the geometry of the multiple images is redshift dependent, we can not only remove stars as main contaminants, but also remove contaminant galaxies at redshifts $\lesssim 3$ by using the constrained lens model to essentially measure a “geometric redshift,” and rule out low redshift false positives. In addition, even if the sources are not multiply imaged, they will likely be highly distorted, allowing one to discriminate them from stellar objects and unlensed lower redshift galaxies.

12.11.3 The Need for a Well-calibrated Telescope

LSST will help us measuring the luminosity function of $z \gtrsim 7$ galaxies by using ~ 1000 galaxy clusters as cosmic telescopes. One will also need J and H -band follow-up imaging to a depth of at least $H_{\text{AB}} = 27.5$, which will require future space-based missions such as JWST. The resulting sample of $\gtrsim 2000$ sources at $z \gtrsim 7$ will allow us to measure the full shape of the luminosity function at $z \gtrsim 7$. Comparing the results with simulations (see e.g., [Choudhury & Ferrara 2007](#)) will allow us to answer the question of whether this population was responsible for reionization.

At $z \sim 3 - 4$, LSST will study the lensed galaxy population to a depth far beyond the luminosities reached by the deepest field surveys (§ 9.7), albeit surveying a substantially smaller solid angle. In combination, these surveys will provide a very accurate luminosity function of Lyman break galaxies (LBGs) from the bright to the faint end.

12.12 Calibrating the LSST Cluster Mass Function using Strong and Weak Lensing

M. James Jee, Maruša Bradač, Phil Marshall

12.12.1 Introduction

The cluster mass function $dn(M)/dz$ is one of the four most promising dark energy probes that the Dark Energy Task Force (DETF) recommends ([Albrecht et al. 2006](#)). Both growth and expansion rates due to the presence of dark energy sensitively affect the abundance of collapsed structures, and the sensitivity increases toward the high mass end ([Figure 12.22](#)). The cluster counting

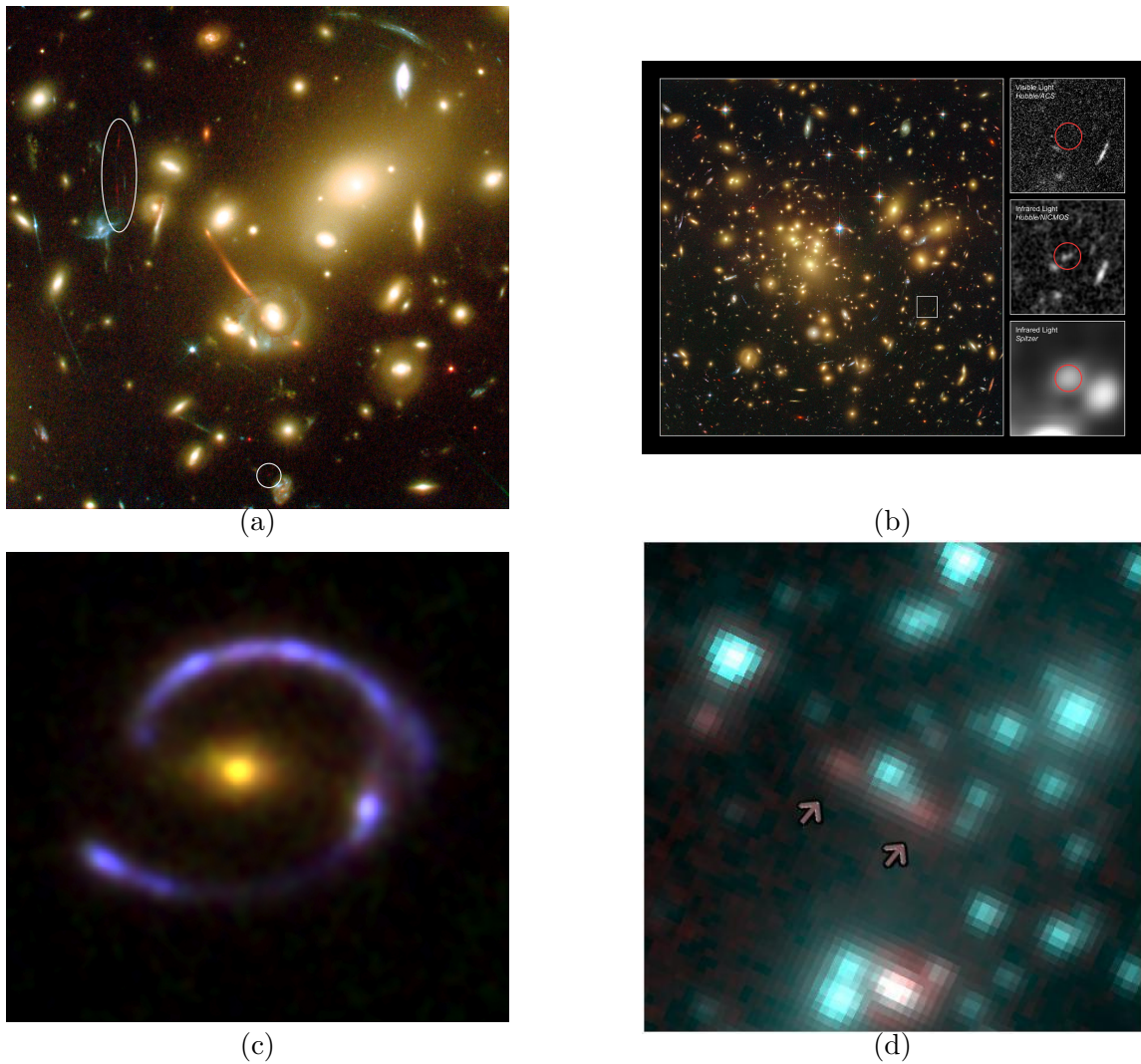


Figure 12.21: (a) This close-up of the galaxy cluster Abell 2218 shows a $z \sim 7$ galaxy that was magnified by the cluster acting as a gravitational telescope (Kneib et al. 2004). (b) $z \sim 7.6$ galaxy behind A1689 (Bradley et al. 2008). (c) LBG J2135-0102 (also known as the “Cosmic Eye”) is a typical star-forming galaxy at $z = 3.07$. Resolved spectroscopy was made possible for this high redshift, regular star-forming galaxy because of the magnifying power of the foreground galaxy (Smail et al. 2007). (d) Bright IRAC (shown) and sub-mm source at a redshift of $z = 2.7$, lensed by the Bullet Cluster (Gonzalez et al. 2009).

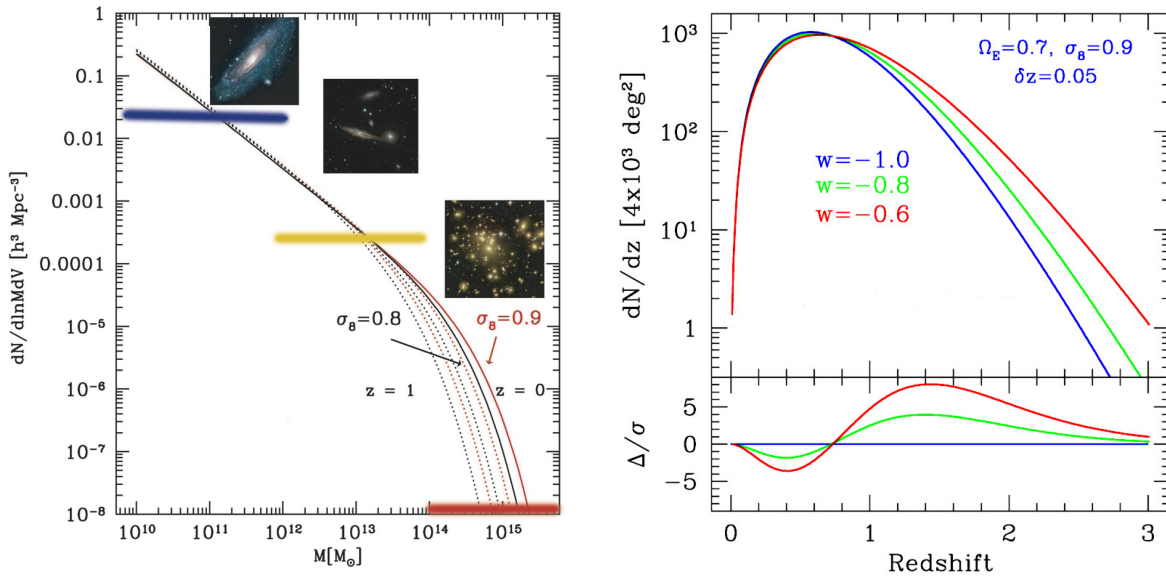


Figure 12.22: *Left*: schematic representation of the dependence of mass function on cosmological parameter σ_8 . The sensitivity to cosmological parameters is highest at the high-mass end. *Right*: the number of clusters above an observable mass threshold as a function of redshift for different values of dark energy equation-of-state parameter w (Mohr 2005). The volume effect is dominant at $z \sim 0.5$ whereas the growth rate sensitivity determines the cluster numbers at $z \sim 1.5$.

cosmology experiment is introduced in § 13.6, which we recommend be read for context for the present discussion. In this section we discuss the contribution that strong lensing can make towards a better calibrated cluster mass function.

Most of the galaxy clusters in the high mass regime have core surface densities high enough to create conspicuous strong lensing features such as multiple images, arcs, and arclets. A critical curve, whose location depends on the source redshift, defines the aperture inside which the total projected mass becomes unity². Therefore, more than one multiple image system at significantly different redshifts enables us to obtain an absolutely calibrated mass profile. The superb image resolution of LSST, as well as the deep six-band data, will facilitate the identification of multiple systems, which can be automated by robotic searches (e.g., Marshall et al. 2009). Still, not all clusters will show strong lensing features; we can expect a sub-set of all weak lensing or optically selected clusters to be suitable for strong plus weak lensing mass measurement. How this “calibration set” should be optimally combined with the larger sample is a topic for research.

An absolutely calibrated mass profile is useful for revealing systematic errors in weak lensing such as shear calibration, source redshift estimation, PSF modeling, and so on. Even when the cluster field does not reveal more than one multiple image system at different redshifts, the ellipticity of the strongly distorted galaxies can put strong constraints on the mass slope, again because there are many such arclets sampling the gravitational field at many radii. Once properly calibrated through the above method, the signal strength is often comparable to that from strong lensing. Therefore, the slope ambiguity arising from using only a single multiple image system can be effectively lifted by including the more numerous arclets, which sample the location of the critical

²Here the mass is defined in units of the critical density Σ_{crit} defined in Equation 12.8.

curves at different redshifts. Currently, one of the major obstacles in this approach is the lack of reliable redshift information for the individual sources: the well-calibrated photometric redshifts needed for LSST weak lensing studies should enable robust statistical cluster analyses as well.

The most significant merit of LSST in cluster mass estimation lies in its ability to measure shears even a few Mpc away from the cluster center (see [Chapter 14](#)) thanks to its unprecedentedly large field of view. Because the mass-sheet degeneracy ($\kappa \rightarrow \lambda\kappa + (1 - \lambda)$) is small in the low κ ($\ll 1$) region, weak lensing cluster masses from LSST (estimated with e.g., aperture mass densitometry ([Fahlman et al. 1994](#)) or some variation [Clowe et al. e.g., 1998](#)) should be relatively free of this effect. In any case, if the weak lensing data are combined with strong lensing constraints, the mass-sheet degeneracy can be broken in the intermediate regime (where κ is not close to zero) because the redshift distribution of the source galaxies serves as an alternative source plane different from the one defined by the strong lensing galaxies (see [Figure 12.23](#) for an example).

Of course, the tangential shears around the cluster at a few Mpc are non-negligibly contaminated by cosmic shear and thus without correcting the effect, it is not feasible to reduce the total halo mass uncertainty to smaller than $\sim 10\%$ ([Hoekstra 2003](#)); extending the field beyond the 10–15 arcmin radius does not decrease the uncertainty. However, considering the ever improving photometric redshift techniques ([§ 3.8](#)) and the LSST wavelength coverage from ultraviolet to near-infrared with significant depth, we anticipate that future tomographic weak lensing analysis ([Hu 2002](#)) will provide a high quality, three-dimensional map of the target field and enable us to separate the cluster mass from the background structure. How well we will be able to do this in practice can be determined from ray tracing simulations: such a program will yield a quantified cluster detection function, essential for accurate cosmology studies.

The LSST weak lensing survey will enable the detection of tens of thousands of clusters over a wide mass range ([§ 14.3.7](#)), the number showing detectable strong lensing signatures will be lower. While the highest mass clusters will contain many arcs, clusters of all masses will be represented in the strong lens sample. LSST will detect $\gtrsim 1000$ clusters with giant arcs ([§ 12.2](#)), and so provide efficient, unbiased probes of these cluster masses from the cluster core (10–100 kpc) to well beyond the virial radius ($\gg 1$ Mpc). This will offer a unique opportunity to study the cluster dynamics in unprecedented detail, to construct a well-calibrated mass function, and thus to quantify the effects of dark energy.

12.12.2 Science with LSST Data Alone

Most of the calibration methods above can be implemented without follow-up data. We can summarize the cluster mass function science program in the following steps:

- Cluster search with red-sequence and/or weak lensing analysis. This should provide a well-understood sample of clusters, selected by mass and/or richness (see [§ 13.6](#) and [§ 14.3.7](#) for discussion of these selection techniques).
- Multiple image identification with morphology and color based on initial mass model. With current data, this step is carried out by hand: with such a large sample of clusters, we can either a) enlist many more lensing analysts to do the image identification (see [§ 12.13](#)) or b) attempt to automate the process.

- Shear calibration from the comparison with the strong-lensing constraints in the non-linear regime. This requires a good strong lensing mass model, based on the identified multiple-images, which are the end-product of the previous step.
- Mass distribution estimation. This can be done with the parametrized models built up during the image identification process, or by moving to more flexible grid-based methods. Since the shear calibration was carried out using the strong plus weak lensing data, the major remaining source of systematic error is in the choice of mass model parametrization, and thus it makes sense to use several approaches to probe this systematics.
- Construction of cluster mass function, based on the different mass modeling methods. Accurate uncertainties on the cluster masses will be important, especially in clusters lying close to the mass threshold.
- The mass functions obtained in the previous step at different redshifts are used to quantify dark energy via the evolution of the cluster mass function (§ 13.6). Statistical inference of the mean density profile, concentration-mass relation, and so on can be carried out simultaneously (see § 12.10 for more discussion of this project).

12.12.3 Science Enabled by Follow-up Observations

Although the above science can be carried out with LSST alone, follow-up observations provide important cross-checks on systematics:

- Spectroscopic observations will confirm the multiple image identification, as well as improve upon the photometric redshift obtained from the LSST photometry. Large optical telescopes with multi-object spectrographs will be required: exploring synergies with spectroscopic surveys may be worthwhile, since observing more than a few tens of clusters may be impractical.
- X-ray analysis of the clusters detected by LSST will determine the bias factor present in the X-ray mass estimation method, and suggest an improved approach to convert the X-ray observables into cluster masses. Detailed comparison of gas density and temperature structure with the mass maps per se provides a crucial opportunity to learn about cluster physics and perhaps the properties of dark matter.
- Near-infrared follow-up would improve the accuracy of the arc photometric redshifts, and thus enhance our ability to break the mass-sheet/slope ambiguity. Imaging at high resolution with JWST should provide better arc astrometry and morphology (to confirm the multiple image identification). More lensed features should also come into view, as small, faint, high redshift objects come into view.

12.12.4 Technical Feasibility

The idea of utilizing both strong and weak lensing data simultaneously in a single mass reconstruction is not new (e.g., [Abdelsalam et al. 1998](#)), and the technique has improved substantially in the past decade to the point where reconstructing cluster mass distributions on adaptive pixelized grids is now possible ([Bradač et al. 2006](#); [Jee et al. 2007](#)). Mass distribution parameters (surface

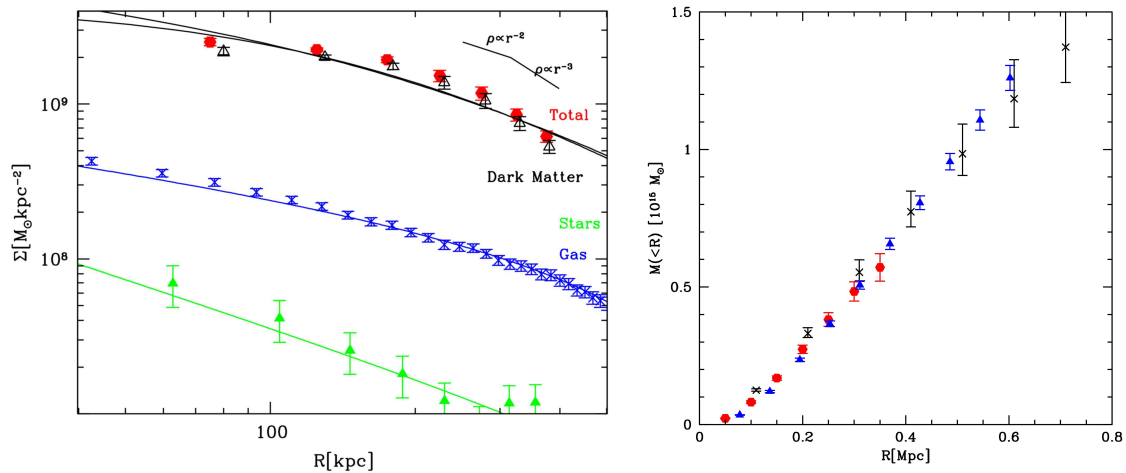


Figure 12.23: *Left:* the projected mass density Σ profile of RX J1347–1145 showing separately the stellar mass profile (filled triangles – green), the gas profile (stars – blue), dark matter profile (open triangles – black) and the total profile from strong and weak lensing (hexagons – red). The dark matter profile has been fitted using the generalized NFW model - shown is the best fit model (inner slope $\beta = 0$, scale radius $r_s = 160\text{kpc}$), and also a best fit NFW model ($\beta = 1$, $r_s = 350\text{kpc}$). We combine with constraints on larger scale (from weak lensing) we will be able to break these degeneracies. *Right:* Comparison of the projected total mass profiles for RX J1347–1145 determined from the strong-plus-weak lensing analysis (red hexagons), the Chandra X-ray data (black crosses), and strong lensing analysis where a profile slope has been assumed (blue triangles). The presence of significant non-thermal pressure support would cause the X-ray measurements to underestimate the total mass. Data from Bradač et al. 2008b.

density, or lens potential, pixel values) are inferred from the data via a joint likelihood, consisting of the product of a weak lensing term with a strong lensing term. Although the exploration and optimization of the thousands of parameters (e.g., a mass/potential 50×50 grid has 2,500 parameters to be constrained) involved is certainly a CPU-intensive operation, future parallelization of the mass reconstruction algorithm will overcome this obstacle and allow us to significantly extend the grid size limits. Automatic searches for multiple images have been implemented for galaxy-scale lenses (Marshall et al. 2009). Although a significant fraction of the machine-identified candidates will need to be individually confirmed by human eyes, it still dramatically exceeds the purely manual identification rate. Adapting this to cluster scale will require an iterative scheme, mimicking the current human approach of trial-and-error cluster modeling. The central principle will remain; however, confirmation of a lensing event requires a successful mass model.

12.13 Education and Public Outreach

Phil Marshall

In this final section we give brief outlines of two possible EPO projects connected to strong lensing science. Both are based around the “Galaxy Zoo” concept described in the Galaxies and EPO chapters (§ 9.11 and § 4.5 respectively).

12.13.1 Finding Complex Lenses

Simple galaxy-scale lenses and giant arcs can be found using automated detection routines. However, more exotic lenses are more difficult to find. Group-scale lenses may contain a lot of confusing lens-plane structure, while arguably the most interesting lenses are the ones least likely to be found by robots trained on more typical lenses. To date, many complex lenses have been found by eyeball inspection of images – this process can be continued into the LSST era provided we increase the number of eyeballs accordingly. The Citizen Science website, Galaxy Zoo, has, at the time of writing, a community of over 200,000 people enthusiastically inspecting images of galaxies and classifying their morphology. Systematic lens-finding will be a feature of the second generation “Zoo2” site, from which we will learn much about how the process of lens detection and identification can be “crowd-sourced.” Starting from the simple tutorial and decision tree of Zoo2, we can imagine moving on from simple lens configurations and building up to the truly exotic lenses in time for LSST. Interestingly, the Galaxy Zoo forum thread, “Are these gravitational lenses,” is after a promising beginning already overflowing with low-probability lens candidates, illustrating the need for well-designed tutorials and sources of more information. This is the motivation for the second Galaxy Zoo strong lensing EPO project.

Eyeball classification works on color JPG images made from cutout “postage stamp” images. Ideally, these images will represent the optimal resolution and signal-to-noise ratio available. We might consider providing deconvolved images (where the deconvolution is performed in a stable, inferential way) as a way of increasing the resolution over the basic stacked images, but this will incur a significant image processing overhead. Even at 1 sec per cutout, deconvolving the 10^8 bright, massive galaxies detected by LSST would take 3.2 CPU-years (12 days on a 100-CPU farm).

12.13.2 Modeling Gravitational Lenses by Hand

A key feature of the previous project is that it touches a particular nerve of the Citizen Science community: the strong desire to be the first to discover a new and exciting celestial object. Still, the bulk of the Galaxy Zoo classifications will be done (it seems) by infrequent or low attention span users, whose drive for discovery wanes after ~ 100 galaxy inspections. However, there is a particular class of Zooites who actively want to spend time investigating a smaller number of systems in some detail, and spend significant amounts of time and energy learning about new things that are posted to the discussion forums (often from each other). We can think of reaching this community not just by providing more data, but better tools with which to investigate the interesting subset of data they have themselves distilled from the survey. We propose to have this team perform the necessary “expert” human classification of lens candidates generated in the first project above.

The only difference between professional gravitational lens astrophysicists and the amateur astronomers of the Galaxy Zoo community is that the former are able, through experience and physical intuition, to quickly assess a lens candidate’s status: they do this by essentially modeling the system as a lens in their heads, and rejecting objects that do not fit. The Zooites will be able to do this just as well, if they are provided with a *tool for modeling gravitational lenses*. We can imagine a web interface where the model parameters can be dialed up and down, and the

corresponding predicted image displayed and compared with the LSST object postage stamp in real time.

This modeling process will not only yield a much purer sample of new complex lenses, it will also provide an excellent platform for teaching scientific data analysis and inference in the classroom. It will introduce the key concept of fitting a model to data in a very clear and, one hopes, satisfying way. One can imagine basing a high school lesson series or an undergraduate laboratory exercise on this tool.

References

- Aarseth, S. J., & Fall, S. M., 1980, *ApJ*, 236, 43
- Abdelsalam, H. M., Saha, P., & Williams, L. L. R., 1998, *AJ*, 116, 1541
- Albrecht, A. et al., 2006, ArXiv Astrophysics e-prints, arXiv:astro-ph/0609591
- Baldry, I. K., & Glazebrook, K., 2003, *ApJ*, 593, 258
- Barkana, R., 1997, *ApJ*, 489, 21
- Barnes, J., 1985, *MNRAS*, 215, 517
- Biggs, A. D., Browne, I. W. A., Helbig, P., Koopmans, L. V. E., Wilkinson, P. N., & Perley, R. A., 1999, *MNRAS*, 304, 349
- Bolton, A. S., Burles, S., Koopmans, L. V. E., Treu, T., Gavazzi, R., Moustakas, L. A., Wayth, R., & Schlegel, D. J., 2008, *ApJ*, submitted
- Bolton, A. S., Burles, S., Koopmans, L. V. E., Treu, T., & Moustakas, L. A., 2006, *ApJ*, 638, 703
- Bouwens, R. J., Illingworth, G. D., Franx, M., & Ford, H., 2008, *ApJ*, 686, 230
- Bradač, M., Allen, S. W., Treu, T., Ebeling, H., Massey, R., Morris, R. G., von der Linden, A., & Applegate, D., 2008a, *ApJ*, 687, 959
- Bradač, M. et al., 2006, *ApJ*, 652, 937
- , 2008b, *ApJ*, 681, 187
- Bradley, L. D. et al., 2008, *ApJ*, 678, 647
- Broadhurst, T. et al., 2005, *ApJ*, 621, 53
- Burud, I. et al., 2002a, *A&A*, 383, 71
- , 2002b, *A&A*, 391, 481
- , 2000, *ApJ*, 544, 117
- Burud, I., Magain, P., Sohy, S., & Hjorth, J., 2001, *A&A*, 380, 805
- Cabanac, R. A. et al., 2007, *A&A*, 461, 813
- Chiba, M., 2002, *ApJ*, 565, 17
- Choi, Y.-Y., Park, C., & Vogeley, M. S., 2007, *ApJ*, 658, 884
- Choudhury, T. R., & Ferrara, A., 2007, *MNRAS*, 380, L6
- Clowe, D., Bradač, M., Gonzalez, A. H., Markevitch, M., Randall, S. W., Jones, C., & Zaritsky, D., 2006, *ApJL*, 648, L109
- Clowe, D., Luppino, G. A., Kaiser, N., Henry, J. P., & Gioia, I. M., 1998, *ApJL*, 497, L61
- Coe, D., & Moustakas, L., 2009, ArXiv e-prints, 0906.4108
- Colley, W. N., & Schild, R. E., 2003, *ApJ*, 594, 97
- Congdon, A. B., Keeton, C. R., & Nordgren, C. E., 2009, *ApJ*, submitted
- Courbin, F., Lidman, C., Frye, B. L., Magain, P., Broadhurst, T. J., Pahre, M. A., & Djorgovski, S. G., 1998, *ApJL*, 499, L119
- Dai, X., & Kochanek, C. S., 2008, ArXiv e-prints, 0803.1679
- Dalal, N., 2005, in 25 Years After the Discovery: Some Current Topics on Lensed QSOs, L. J. Goicoechea, ed.
- Dalal, N., & Kochanek, C. S., 2002, *ApJ*, 572, 25
- Diego, J. M., Tegmark, M., Protopapas, P., & Sandvik, H. B., 2005, ArXiv e-prints astro-ph/0509103
- Diemand, J., Kuhlen, M., Madau, P., Zemp, M., Moore, B., Potter, D., & Stadel, J., 2008, *Nature*, 454, 735
- Draine, B. T. et al., 2007, *ApJ*, 663, 866
- Dunkley, J. et al., 2008, ArXiv e-prints, 0803.0586
- Eke, V. R. et al., 2004, *MNRAS*, 355, 769

- Elíasdóttir, Á. et al., 2008, ArXiv e-prints, 0810.2897
- Elíasdóttir, Á., Hjorth, J., Toft, S., Burud, I., & Paraficz, D., 2006, *ApJS*, 166, 443
- Ellis, R., Santos, M. R., Kneib, J.-P., & Kuijken, K., 2001, *ApJL*, 560, L119
- Ellison, S. L., Hall, P. B., & Lira, P., 2005, *AJ*, 130, 1345
- Fahlman, G., Kaiser, N., Squires, G., & Woods, D., 1994, *ApJ*, 437, 56
- Falco, E. E. et al., 1999, *ApJ*, 523, 617
- Fassnacht, C. D., 1999, PhD thesis, California Institute of Technology
- Fassnacht, C. D., Kocevski, D. D., Auger, M. W., Lubin, L. M., Neureuther, J. L., Jeltama, T. E., Mulchaey, J. S., & McKean, J. P., 2008, *ApJ*, 681, 1017
- Fassnacht, C. D. et al., 2006, *ApJ*, 651, 667
- Fassnacht, C. D., Xanthopoulos, E., Koopmans, L. V. E., & Rusin, D., 2002, *ApJ*, 581, 823
- Faure, C. et al., 2008, *ApJS*, 176, 19
- Gal, R. R., Lemaux, B. C., Lubin, L. M., Kocevski, D., & Squires, G. K., 2008, *ApJ*, 684, 933
- Geller, M. J., & Huchra, J. P., 1983, *ApJS*, 52, 61
- Gnedin, O. Y., Kravtsov, A. V., Klypin, A. A., & Nagai, D., 2004, *ApJ*, 616, 16
- Goicoechea, L. J., Gil-Merino, R., & Ullán, A., 2005, *MNRAS*, 360, L60
- Gonzalez, A. H., Clowe, D., Bradač, M., Zaritsky, D., Jones, C., & Markevitch, M., 2009, *ApJ*, 691, 525
- Henry, A. L., Malkan, M. A., Colbert, J. W., Siana, B., Teplitz, H. I., McCarthy, P., & Yan, L., 2007, *ApJL*, 656, L1
- Hjorth, J. et al., 2002, *ApJL*, 572, L11
- Hoekstra, H., 2003, *MNRAS*, 339, 1155
- Hopkins, A. M., & Beacom, J. F., 2006, *ApJ*, 651, 142
- Hopkins, P. F. et al., 2004, *AJ*, 128, 1112
- Hu, E. M., Cowie, L. L., McMahan, R. G., Capak, P., Iwamuro, F., Kneib, J.-P., Maihara, T., & Motohara, K., 2002, *ApJL*, 568, L75
- Hu, W., 2002, *Phys. Rev. D*, 66, 083515
- Inada, N. et al., 2003, *Nature*, 426, 810
- Jakobsson, P. et al., 2004, *A&A*, 427, 785
- Jee, M. J. et al., 2007, *ApJ*, 661, 728
- Jeltama, T. E., Mulchaey, J. S., Lubin, L. M., & Fassnacht, C. D., 2007, *ApJ*, 658, 865
- Jeltama, T. E., Mulchaey, J. S., Lubin, L. M., Rosati, P., & Böhringer, H., 2006, *ApJ*, 649, 649
- Keeton, C. R., 2009a, preprint arXiv:0908.3001
- , 2009b, in Identification of Dark Matter 2008, J. Edsjo, ed., Proceedings of Science
- Keeton, C. R., Burles, S., Schechter, P. L., & Wambsganss, J., 2006, *ApJ*, 639, 1
- Keeton, C. R., Gaudi, B. S., & Petters, A. O., 2003, *ApJ*, 598, 138
- , 2005, *ApJ*, 635, 35
- Keeton, C. R., & Moustakas, L. A., 2009, *ApJ*, 699, 1720
- Keeton, C. R., & Zabludoff, A. I., 2004, *ApJ*, 612, 660
- Keeton, C. R., Chartas, G., Roodman, A., Dobler, G., Fassnacht, C., Marshall, P., Oguri, M., & LSST Strong Lensing Science Collaboration, 2009, Bulletin of the American Astronomical Society, Vol. 41, LSST Strong Lensing: Galaxies And Their Nuclei Under A Gravitational Microscope. p. 369
- Kneib, J. et al., 2003, *ApJ*, 598, 804
- Kneib, J.-P., Ellis, R. S., Santos, M. R., & Richard, J., 2004, *ApJ*, 607, 697
- Kochanek, C. S., 2002, *ApJ*, 578, 25
- , 2006, in Gravitational Lensing: Strong, Weak & Micro, G. Meylan, P. Jetzer, & P. North, eds., Lecture Notes of the 33rd Saas-Fee Advanced Course, Springer-Verlag: Berlin
- Kochanek, C. S., Mochejska, B., Morgan, N. D., & Stanek, K. Z., 2006a, *ApJL*, 637, L73
- Kochanek, C. S., Morgan, N. D., Falco, E. E., McLeod, B. A., Winn, J. N., Dembicky, J., & Ketzeback, B., 2006b, *ApJ*, 640, 47
- Koopmans, L. V. E., de Bruyn, A. G., Xanthopoulos, E., & Fassnacht, C. D., 2000, *A&A*, 356, 391
- Koopmans, L. V. E., Treu, T., Bolton, A. S., Burles, S., & Moustakas, L. A., 2006, *ApJ*, 649, 599
- Koopmans, L. V. E., Treu, T., Fassnacht, C. D., Blandford, R. D., & Surpi, G., 2003, *ApJ*, 599, 70
- Kormann, R., Schneider, P., & Bartelmann, M., 1994, *A&A*, 284, 285
- Krisciunas, K., Hastings, N. C., Loomis, K., McMillan, R., Rest, A., Riess, A. G., & Stubbs, C., 2000, *ApJ*, 539, 658
- Kundić, T. et al., 1995, *ApJL*, 455, L5
- , 1997, *ApJ*, 482, 75

- Limousin, M. et al., 2008, ArXiv e-prints, 0812.1033
—, 2007, *ApJ*, 668, 643
Linder, E. V., 2004, *Phys. Rev. D*, 70, 043534
Lovell, J. E. J., Jauncey, D. L., Reynolds, J. E., Wieringa, M. H., King, E. A., Tzioumis, A. K., McCulloch, P. M., & Edwards, P. G., 1998, *ApJL*, 508, L51
Lynds, R., & Petrosian, V., 1986, Bulletin of the American Astronomical Society, Vol. 18, Giant Luminous Arcs in Galaxy Clusters. p. 1014
Madau, P., Haardt, F., & Rees, M. J., 1999, *ApJ*, 514, 648
Malhotra, S., 1997, *ApJL*, 488, L101
Marshall, P. J., Hobson, M. P., Gull, S. F., & Bridle, S. L., 2002, *MNRAS*, 335, 1037
Marshall, P. J., Hogg, D. W., Moustakas, L. A., Fassnacht, C. D., Bradač, M., Schrabback, T., & Blandford, R. D., 2009, *ApJ*, 694, 924
McKean, J. P. et al., 2007, *MNRAS*, 378, 109
Medezinski, E., Broadhurst, T., Umetsu, K., Oguri, M., Rephaeli, Y., & Benítez, N., 2009, ArXiv e-prints, 0906.4791
Merritt, D., 1985, *ApJ*, 289, 18
Metcalf, R. B., & Madau, P., 2001, *ApJ*, 563, 9
Mitchell, J. L., Keeton, C. R., Frieman, J. A., & Sheth, R. K., 2005, *ApJ*, 622, 81
Mohr, J. J., 2005, in Astronomical Society of the Pacific Conference Series, Vol. 339, Observing Dark Energy, S. C. Wolff & T. R. Lauer, eds., p. 140
Momcheva, I., Williams, K., Keeton, C., & Zabludoff, A., 2006, *ApJ*, 641, 169
Morokuma, T. et al., 2007, *AJ*, 133, 214
Mosquera, A. M., Muñoz, J. A., & Mediavilla, E., 2008, ArXiv e-prints, 0810.1626
Moustakas, L. A. et al., 2007, *ApJL*, 660, L31
Muñoz, J. A., Falco, E. E., Kochanek, C. S., McLeod, B. A., & Mediavilla, E., 2004, *ApJ*, 605, 614
Mulchaey, J. S., Lubin, L. M., Fassnacht, C., Rosati, P., & Jeltama, T. E., 2006, *ApJ*, 646, 133
Mulchaey, J. S., & Zabludoff, A. I., 1998, *ApJ*, 496, 73
Murphy, M. T., & Liske, J., 2004, *MNRAS*, 354, L31
Nagai, D., Kravtsov, A. V., & Vikhlinin, A., 2007, *ApJ*, 668, 1
Nakajima, R., Bernstein, G. M., Fadely, R., Keeton, C. R., & Schrabback, T., 2009, ArXiv e-prints, 0903.4182
Natarajan, P., & Kneib, J.-P., 1996, *MNRAS*, 283, 1031
Navarro, J. F., Frenk, C. S., & White, S. D. M., 1997, *ApJ*, 490, 493
Oda, T., & Totani, T., 2005, *ApJ*, 630, 59
Oguri, M., 2006, *MNRAS*, 367, 1241
—, 2007, *ApJ*, 660, 1
Oguri, M., & Blandford, R. D., 2009, *MNRAS*, 392, 930
Oguri, M. et al., 2009, *ApJ*, 699, 1038
—, 2006, *AJ*, 132, 999
Oguri, M., & Kawano, Y., 2003, *MNRAS*, 338, L25
Oguri, M. et al., 2008, *AJ*, 135, 512
Orban de Xivry, G., & Marshall, P., 2009, ArXiv e-prints, 0904.1454
Osmond, J. P. F., & Ponman, T. J., 2004, *MNRAS*, 350, 1511
Paczynski, B., & Wambsganss, J., 1989, *ApJ*, 337, 581
Pei, Y. C., Fall, S. M., & Bechtold, J., 1991, *ApJ*, 378, 6
Pelt, J., Hoff, W., Kayser, R., Refsdal, S., & Schramm, T., 1994, *A&A*, 286, 775
Pelt, J., Kayser, R., Refsdal, S., & Schramm, T., 1996, *A&A*, 305, 97
Perlmutter, S. et al., 1997, *ApJ*, 483, 565
Press, W. H., Rybicki, G. B., & Hewitt, J. N., 1992a, *ApJ*, 385, 404
—, 1992b, *ApJ*, 385, 416
Randall, S. W., Markevitch, M., Clowe, D., Gonzalez, A. H., & Bradač, M., 2008, *ApJ*, 679, 1173
Refsdal, S., 1964, *MNRAS*, 128, 307
Richard, J., Pelló, R., Schaerer, D., Le Borgne, J.-F., & Kneib, J.-P., 2006, *A&A*, 456, 861
Richards, G. T. et al., 2006, *AJ*, 131, 2766
Riess, A. G. et al., 1998, *AJ*, 116, 1009
Riess, A. G., Press, W. H., & Kirshner, R. P., 1996, *ApJ*, 473, 588
Rusin, D., & Kochanek, C. S., 2005, *ApJ*, 623, 666
Sand, D. J., Treu, T., Ellis, R. S., Smith, G. P., & Kneib, J.-P., 2008, *ApJ*, 674, 711

- Schechter, P. L., & Wambsganss, J., 2002, *ApJ*, 580, 685
- Schneider, P., 2006, in *Gravitational Lensing: Strong, Weak & Micro*, G. Meylan, P. Jetzer, & P. North, eds., Lecture Notes of the 33rd Saas-Fee Advanced Course, Springer-Verlag: Berlin
- Shin, E. M., & Evans, N. W., 2008, *MNRAS*, 385, 2107
- Smail, I. et al., 2007, *ApJL*, 654, L33
- Soucail, G., 1990, *APSS*, 170, 283
- Soucail, G., Fort, B., Mellier, Y., & Picat, J. P., 1987, *A&A*, 172, L14
- Springel, V. et al., 2008, *MNRAS*, 391, 1685
- Stanway, E. R., Bremer, M. N., Squitieri, V., Douglas, L. S., & Lehnert, M. D., 2008, *MNRAS*, 386, 370
- Stark, D. P., Ellis, R. S., Richard, J., Kneib, J.-P., Smith, G. P., & Santos, M. R., 2007, *ApJ*, 663, 10
- Sullivan, M. et al., 2006, *ApJ*, 648, 868
- Treu, T., & Koopmans, L. V. E., 2004, *ApJ*, 611, 739
- Trott, C. M., Treu, T., Koopmans, L. V. E., & Webster, R. L., 2008, ArXiv e-prints, 0812.0748
- Turner, E. L., & Gott, III, J. R., 1976, *ApJS*, 32, 409
- Turner, E. L., Ostriker, J. P., & Gott, III, J. R., 1984, *ApJ*, 284, 1
- Vuissoz, C. et al., 2008, *A&A*, 488, 481
- , 2007, *A&A*, 464, 845
- Walsh, D., Carswell, R. F., & Weymann, R. J., 1979, *Nature*, 279, 381
- Wang, X., Wang, L., Pain, R., Zhou, X., & Li, Z., 2006, *ApJ*, 645, 488
- Willis, J. P. et al., 2005, *MNRAS*, 363, 675
- Wilman, D. J., Balogh, M. L., Bower, R. G., Mulchaey, J. S., Oemler, A., Carlberg, R. G., Morris, S. L., & Whitaker, R. J., 2005, *MNRAS*, 358, 71
- Wilson, G. W. et al., 2008, *MNRAS*, 390, 1061
- Wisotzki, L., Becker, T., Christensen, L., Jahnke, K., Helms, A., Kelz, A., Roth, M. M., & Sánchez, S. F., 2004, *Astronomische Nachrichten*, 325, 135
- Wucknitz, O., Wisotzki, L., Lopez, S., & Gregg, M. D., 2003, *A&A*, 405, 445
- York, D. G. et al., 2006, *MNRAS*, 367, 945
- Zabludoff, A. I., & Mulchaey, J. S., 1998, *ApJ*, 496, 39
- Zentner, A. R., & Bullock, J. S., 2003, *ApJ*, 598, 49
- Zhan, H., Knox, L., & Tyson, J. A., 2009, *ApJ*, 690, 923